Composite Structures 389 (2026) 120444

Contents lists available at ScienceDirect

Composite Structures

journal homepage: www.elsevier.com/locate/compstruct

A unified Ritz framework for free vibration analysis of shells

F.A.X.C. Pinho [a,c,*], F.M.A. Silva [b], F.A.C. Monteiro [c], M. Amabili [d,e], C.G. Pitaluga [b]

[a] Faculdade de Tecnologia, Universidade de Brasília, 70910-900, Brasília, DF, Brazil
[b] Escola de Engenharia Civil e Ambiental, Universidade Federal de Goiás, 74605-220, Goiânia, GO, Brazil
[c] Centro de Ciências e Tecnologia, Universidade Federal do Cariri, 63048-080, Juazeiro do Norte, CE, Brazil
[d] School of Engineering, Westlake University, Hangzhou, Zhejiang province, PR China
[e] Department of Mechanical Engineering, McGill University, QC H3A 2T7, Montreal, QC, Canada

ARTICLE INFO

Dataset link: ShellPy: A Python framework for general shell analysis (Original data)

Keywords:
Ritz method
Büchter–Ramm–Roehl shell theory
Doubly curved shells
Composite shells
Enriched trigonometric set

ABSTRACT

This paper presents a unified Ritz-based framework for the free vibration analysis of shells, integrating symbolic and numerical computation to automatically evaluate shell geometry from its position vector. Unlike many existing Ritz-based models that are restricted to specific shell geometries, the proposed approach overcomes these case-specific limitations by automating the derivation of differential geometry parameters, enabling the analysis of a broad range of shapes within a single formulation. It employs enriched trigonometric sets to handle various boundary conditions. The modular framework allows comparison of different kinematic models, where a seven-parameter formulation with Enhanced Assumed Strain effectively mitigates locking effects in moderately thick shells. A key advantage of this methodology is its high computational efficiency, achieving converged results with significantly fewer degrees of freedom compared to high-fidelity 3D finite element models. While current applications are focused on linear problems within regular computational domains, the formulation is conceived to enable future extensions to complex nonlinear analyses. The formulation robustness is demonstrated by numerical examples on functionally graded and laminated composites, showing strong agreement with 3D finite element models.

1. Introduction

Shell structures are widely used in aerospace, civil, mechanical, and maritime engineering due to their high spatial efficiency and superior strength-to-weight ratio. Their load-carrying capacity is primarily governed by curvature effects, allowing lightweight and high-performance structural designs. Recent advances in material science have significantly increased interest in the analysis of general composite shells made of anisotropic laminates or functionally graded materials, requiring refined formulations [1–4].

Historically, shell theories have evolved to address the limitations of classical formulations. Classical shell theory (CST), based on the Kirchhoff–Love hypothesis, neglects transverse shear deformation and is consequently restricted to thin shells undergoing small strains and moderate rotations [1,3,4]. To incorporate transverse shear effects in moderately thick and composite shells, first-order shear deformation theory (FSDT) was developed, characterizing shell kinematics by five independent fields and generally assuming a plane stress state through the thickness [4–6]. Several challenges related to nonlinear vibrations, stability phenomena, and the mechanical behavior of advanced composite and biological shell structures have been systematically studied, establishing a robust theoretical basis for refined kinematic models [7,8]. To further overcome the limitations of FSDT and reduce dependence on shear correction factors, higher-order shear deformation theory (HSDT) and layer-wise (LW) models have been introduced. These enrich the through-thickness displacement field, allowing for a more accurate representation of transverse shear stresses [3–5]. Although HSDT and LW formulations deliver high-fidelity three-dimensional stress predictions for multilayered shells, their computational cost can become considerable in nonlinear analyses due to the increased number of kinematic parameters and independent fields required to capture through-thickness behavior [9–11].

Over the last decade, the CST, FSDT and HSDT have been extensively employed in the analysis of advanced shell structures with increasing geometrical and material complexity. In particular, unified formulation frameworks have enabled the systematic derivation of kinematic models within a single variational setting, allowing consistent comparisons of accuracy and computational efficiency across a wide range of shell problems [12,13]. Such approaches have been successfully applied to static, vibration and stability analyses of laminated, sandwich and functionally graded shells, including cylindrical,

* Corresponding author at: Faculdade de Tecnologia, Universidade de Brasília, 70910-900, Brasília, DF, Brazil.
E-mail address: flavio.pinho@unb.br (F.A.X.C. Pinho).

https://doi.org/10.1016/j.compstruct.2026.120444
Received 12 February 2026; Received in revised form 6 April 2026; Accepted 10 May 2026
Available online 15 May 2026

spherical, and doubly curved configurations [4]. In parallel, refined shear deformation theories have continued to support detailed investigations of nonlinear vibration and post-buckling behavior of shells under large deflections, as extensively documented in contemporary studies on nonlinear shell dynamics [7,8].

Comprehensive treatments of vibration and stability in thin and moderately thick shells, encompassing CPT, FSDT, and HSDT models, affirm the sustained relevance of these theories in modern engineering applications [14]. Spurred by these developments, the application of such models has expanded considerably across a wide range of curved shell geometries and engineering scenarios. For instance, refined FSDT models have been employed to study the free vibration characteristics of honeycomb sandwich shell structures [15], while modified numerical strategies have been introduced for the static and dynamic analysis of laminated conical shells [16]. In the area of structural stability, comprehensive review studies have consolidated the mechanisms governing buckling in curved shells, underscoring the need for high-fidelity theoretical descriptions [17]. Further research efforts have focused on vibration analysis of variable-thickness shallow shells [18,19] and on the dynamic response of functionally graded, porous, and perforated curved structures [20]. Moreover, analytical studies of laminated axisymmetric spherical shells and thick functionally graded spherical structures illustrate the continued pursuit of greater predictive accuracy, particularly regarding interlaminar stress distributions and thermomechanical effects, through refined kinematic theories [21–23]. The accurate implementation of such theories has driven an extensive literature on high-order numerical methods, which are essential for capturing complex deformation phenomena. Among these approaches, Isogeometric Analysis (IGA) has established itself as a versatile tool for advanced shell modeling, enabling everything from the accurate representation of laminates with zigzag effects and efficient coupling in stiffened structures to the analysis of complex nonlinear phenomena such as post-buckling in piezoelectric materials and fluid–structure interaction in turbulent regimes [24–28]. In parallel, the *p*-version of the finite element method (*p*-FEM) allows for exponential convergence by enriching the polynomial order of shape functions within each element rather than refining the mesh, proving particularly efficient for composite and sandwich structures [29,30]. Spectral Element Methods (SEM), including techniques such as the Spectral Chebyshev Technique (SCT), leverage the convergence properties of orthogonal polynomials to significantly reduce the number of degrees of freedom required for accurate solutions [29,31,32]. Furthermore, high-order Discontinuous Galerkin formulations have demonstrated significant adaptability in the analysis of multilayered structures, enabling a tuneable high-order accuracy through both the shell thickness and the modeling domain. Such frameworks have proven robust for handling complex geometric nonlinearities and transient dynamic responses while maintaining computational efficiency compared to traditional 3D finite element solutions [33,34]. Within this context, the Ritz method remains a robust and computationally efficient semi-analytical alternative, offering high-fidelity global approximations for the free vibration and stability problems of shells [24,35]. Collectively, these contributions reaffirm the value of refined two-dimensional theories for curved shell configurations, while also highlighting a growing need for more comprehensive modeling approaches capable of unifying such diverse structural responses within a single theoretical framework.

A more general kinematic framework is offered by six-parameter shell theories. According these formulations, the director vector is represented by its three components, resulting in a fully three-dimensional stress state capable of describing complex deformation modes [5,36]. However, these models are frequently susceptible to locking phenomena, notably thickness locking (or Poisson locking). This occurs because the assumed constant through-thickness distribution of the transverse normal strain cannot accurately represent its linear variation, as required under pure bending [10,11,36]. To overcome this limitation, without resorting to artificial modifications of the material law, seven-parameter shell theories have been developed [9,36,37]. Following the Enhanced Assumed Strain (EAS) technique, the seventh parameter enriches the transverse normal strain field by introducing a linearly varying component through the thickness [11,36,37]. Importantly, this additional parameter can be statically condensed from the discretized global equations. This preserves the efficiency of a displacement-based formulation while enabling the direct use of unmodified three-dimensional constitutive laws [9,11,36].

This work presents a unified Ritz framework for general shell analysis, implemented in the ShellPy library [38], advancing significantly in the unified Ritz framework for shell analysis by building upon the previous works [39–42]. The numerical implementation is extended to encompass a broader class of shell models, including the classical three-parameter theory as well as first-order shear deformation-based five-, six-, and seven-parameter theories. This flexibility allows for the consistent inclusion of transverse shear effects, through appropriate shear correction factors based on the cylindrical bending assumption, the direct use of full three-dimensional constitutive laws without prior stress or strain condensation in addition to thickness stretching. Several constitutive models are supported, enabling the direct modeling of advanced material systems, including functionally graded materials and orthotropic laminated composites. Numerical integration through the thickness and over the shell mid-surface is systematically handled within the formulation, ensuring accuracy and robustness across different kinematic assumptions. Furthermore, the displacement field can be expanded using different Ritz bases, including eigenfunction expansions derived from the free vibration problem of beams, trigonometric series, and polynomial bases such as Legendre and Chebyshev polynomials. In particular, the enriched cosine series [43] presented in this work improves convergence properties and enhances modeling flexibility. Thanks to its modular and extensible design, the proposed framework provides a powerful and versatile tool for the analysis of shells with arbitrary geometry, boundary conditions, and material behavior under linear and dynamic regimes. The numerical results demonstrate the capability of the proposed approach to analyze the free vibration of shells with functionally graded materials and orthotropic laminated composites, showing excellent agreement with three-dimensional finite element solutions and thereby validating both the formulation and its computational implementation. It is emphasized that the novelty of the present contribution resides in the systematic integration of several key aspects within a unified Ritz-based framework. In particular, the proposed approach combines an automatic geometry description derived from the shell position vector, hierarchic enriched trigonometric bases for flexible enforcement of boundary conditions, and the consistent implementation of multiple shell theories within a single modular computational structure. In addition, the framework supports a wide range of material models, allowing the direct analysis of complex heterogeneous structures without the need for case-specific reformulations.

2. Framework formulation

Fig. 1 depicts a moderately thick shell of nonuniform thickness $h(\xi^1,\xi^2)$, embedded in the three-dimensional Euclidean space $\mathbb{E}^3$ spanned by the orthonormal basis vectors $\mathbf{e}_1$, $\mathbf{e}_2$, and $\mathbf{e}_3$. In reference configuration, the shell occupies the region $\mathscr{V} \subset \mathbb{E}^3$. Its mid-surface, denoted by $\mathscr{S}$, is parametrized over a rectangular domain $\Omega \subset \mathbb{R}^2$ with curvilinear coordinates (ξ^1,ξ^2). The parametric space is bounded by $\xi^1_l \leq \xi^1 \leq \xi^1_r$ and $\xi^2_l \leq \xi^2 \leq \xi^2_r$, while the thickness coordinate ξ^3 varies within $-h/2 \leq \xi^3 \leq h/2$ along the direction normal to the reference surface. The position of a point in the reference configuration is expressed as

$$\mathbf{X}(\xi^1,\xi^2,\xi^3) = \mathbf{R}(\xi^1,\xi^2) + \xi^3\mathbf{M}_3(\xi^1,\xi^2) \tag{1}$$

where $\mathbf{R}$ denotes the position vector of the mid-surface, $\mathbf{M}_1$ and $\mathbf{M}_2$ are the tangent vectors to $\mathscr{S}$, and $\mathbf{M}_3$ is the associated unit normal vector satisfying $\mathbf{M}_3 \perp \mathbf{M}_1, \mathbf{M}_2$.

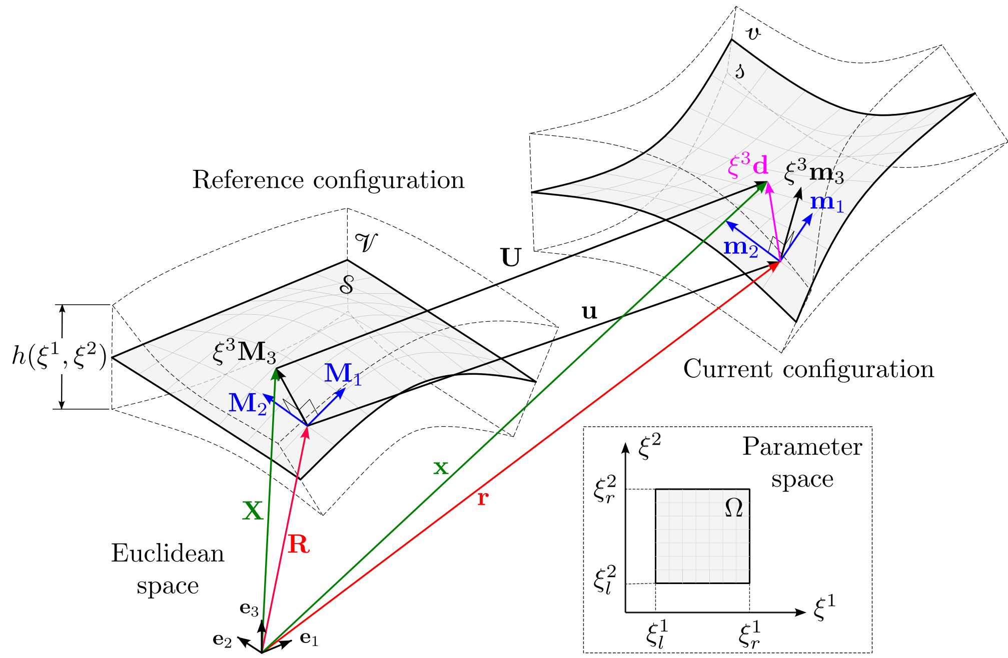

Fig. 1. Schematic of a generic double-curved shell showing the mid-surface in the reference configuration $\mathscr{S}$ (position vector **R**) and in the current configuration $\mathscr{s}$ (position vector **r**). The shell occupies the volumes $\mathscr{V}$ and $\mathscr{v}$, and the thickness coordinate ξ^3 is defined along the unit vector $\mathbf{M}_3$. The displacement vectors of the mid-surface and the shell are **u** and **U**, and the director along the thickness is **d**. The parametric space (ξ^1, ξ^2) used to map the mid-surface is also illustrated.

Table 1
Geometric properties of the shell. Expressions are given for the mid-surface and for a generic point in the shell; detailed formulas are provided in the Appendix.

Geometric property	Mid-surface ($\mathcal{S}$)	Shell ($\mathcal{V}$)
Covariant base vectors	$\mathbf{M}_i$	$\bar{\mathbf{M}}_i$
Contravariant base vectors	$\mathbf{M}^i$	$\bar{\mathbf{M}}^i$
Metric tensor components	$G_{\alpha\beta}$, $G^{\alpha\beta}$	$\bar{G}_{ij}$, $\bar{G}^{ij}$
Curvature tensor components	$K_{\alpha\beta}$, $K^{\beta}_{\cdot\alpha}$	$\bar{K}_{\alpha\beta}$, $\bar{K}^{\beta}_{\cdot\alpha}$
Christoffel symbols	$\Gamma^{\gamma}_{\alpha\beta}$	$\bar{\Gamma}^{k}_{ij}$
Displacement components	u_i, v_i, U_i u^i, v^i, U^i	$\bar{U}_i$, $\bar{U}^i$
Covariant derivatives	$U_{i\|j}$, $U^i\|_j$	$\bar{U}_{i\|\|j}$, $\bar{U}^i\|\|_j$

A detailed description of the geometric properties of the mid-surface and of the shell is provided in the Appendix. These definitions are given both for the mid-surface and for the shell along the thickness, allowing a complete representation of the shell geometry in different bases. For clarity and convenience, Table 1 summarizes the main geometric properties, showing their corresponding quantities for the mid-surface and for a generic point in the shell. Explicit expressions for each property, including metric and curvature tensors, Christoffel symbols, and the covariant derivatives, are provided in the Appendix. Throughout this work, Greek indices $\alpha, \beta \ldots$ range from 1 to 2 (in-plane directions) while Latin indices $i, j \ldots$ range from 1 to 3 (three-dimensional space), a different notation will be explicitly indicated when used.

To relate the basis vectors of the mid-surface and a generic point in the shell along the thickness, the shift tensor $\boldsymbol{\Upsilon} = \Upsilon^{\beta}_{\cdot\alpha}\mathbf{M}_{\beta} \otimes \mathbf{M}^{\alpha}$, with components $\Upsilon^{\beta}_{\cdot\alpha} = \delta^{\beta}_{\alpha} + \xi^3 K^{\beta}_{\cdot\alpha}$, such that $\bar{\mathbf{M}}_{\alpha} = \boldsymbol{\Upsilon} \cdot \mathbf{M}_{\alpha}$, is considered. Similarly, the tensor $\boldsymbol{\Lambda} = \Lambda^{\cdot\alpha}_{\beta}\mathbf{M}^{\beta} \otimes \mathbf{M}_{\alpha}$ relates the contravariant bases of the shell and the mid-surface, i.e. $\bar{\mathbf{M}}^{\alpha} = \boldsymbol{\Lambda} \cdot \mathbf{M}^{\alpha}$. The components of $\boldsymbol{\Lambda}$ are the inverse of those of $\boldsymbol{\Upsilon}$, ensuring consistency between covariant and contravariant representations along the shell thickness. In summary, the bases are related as

$$
\begin{aligned}
\bar{\mathbf{M}}_{\alpha} &= \Upsilon^{\beta}_{\cdot\alpha}\mathbf{M}_{\beta} \qquad & \bar{\mathbf{M}}^{\alpha} &= \Lambda^{\cdot\alpha}_{\beta}\mathbf{M}^{\beta} \\
\mathbf{M}_{\theta} &= \Lambda^{\cdot\alpha}_{\theta}\bar{\mathbf{M}}_{\alpha} \qquad & \mathbf{M}^{\beta} &= \Upsilon^{\beta}_{\cdot\alpha}\bar{\mathbf{M}}^{\alpha}
\end{aligned}
\tag{2}
$$

while the unit normal vectors satisfy $\bar{\mathbf{M}}_3 = \bar{\mathbf{M}}^3 = \mathbf{M}_3 = \mathbf{M}^3$. The detailed derivation of all components and their properties is provided in the Appendix.

2.1. Kinematics of the shell

The kinematics of the shell are described in terms of the displacement fields. The vector **u** represents the displacement of the mid-surface, while **U** denotes the displacement of a generic material point within the volume $\mathscr{V}$. Under a smooth deformation mapping, the shell is carried into the current configuration, where it occupies the region $\mathscr{v}$. In this configuration, the mid-surface is mapped onto $\mathscr{s}$, and the position vector of a generic point is given by $\mathbf{x} = \mathbf{X} + \mathbf{U}$ and the position of the mid-surface is given by $\mathbf{r} = \mathbf{R} + \mathbf{u}$.

Initially, the Reissner–Mindlin assumptions are adopted. Specifically, straight lines initially normal to the reference mid-surface remain straight after deformation, although not necessarily orthogonal to the deformed mid-surface. Nonuniform shell thickness is also accounted for. Within this framework, the displacement field can be expressed as

$$
\mathbf{U} = \mathbf{u} + \xi^3\mathbf{d} - \xi^3\mathbf{M}_3 \tag{3}
$$

where **d**, referred to as the *director vector*, represents the variation of a vector initially normal to the reference mid-surface. Finally, by rearranging terms, the displacement of a generic material point can be conveniently written as

$$
\mathbf{U}(\xi^1, \xi^2, \xi^3) = \mathbf{u}(\xi^1, \xi^2) + \xi^3\mathbf{v}(\xi^1, \xi^2) \tag{4}
$$

where $\mathbf{v} = \mathbf{d} - \mathbf{M}_3$ represents the director variation.

2.2. Shell's deformation

In the following, three different shell theories are presented, each corresponding to a distinct set of assumptions and a different number of independent displacement fields. All three shell theories are implemented within the ShellPy framework, allowing a direct comparison between different kinematic models and enabling flexible numerical analyses depending on the thickness, material behavior, and deformation regime of the shell.

2.2.1. Six-parameter shell theory

Six-parameter shell theory is derived directly from the general kinematic assumptions presented in the previous section. This formulation allows capturing both the in-plane and transverse deformations of the shell consistently with the Reissner–Mindlin hypotheses.

The strain tensor of the shell in curvilinear coordinates is defined in terms of the shell contravariant basis as

$$\mathbf{E} = \bar{E}_{ij}\ \bar{\mathbf{M}}^i \otimes \bar{\mathbf{M}}^j \qquad 2\bar{E}_{ij} = \bar{U}_{i\|j} + \bar{U}_{j\|i} + \bar{U}_{k\|i}\bar{U}^k\|_j \tag{5}$$

where $\bar{E}_{ij}$ denotes the components of the Green–Lagrange strain tensor at a generic point along the thickness. The relations between the covariant derivatives of the shell and the mid-surface can be compactly expressed in terms of the shift tensor and its inverse, $\boldsymbol{\Upsilon}$ and $\boldsymbol{\Lambda}$, with full expressions provided in Appendix. Considering the linearized kinematics, the strain components can be written in terms of the mid-surface displacement $\mathbf{u}$ and the director variation $\mathbf{v}$ as

$$\begin{aligned}
2\bar{E}^{(0)}_{\alpha\beta} &= u_{\alpha|\beta} + u_{\beta|\alpha}\\
2\bar{E}^{(1)}_{\alpha\beta} &= K^{\theta}_{\cdot\alpha}u_{\theta|\beta} + K^{\theta}_{\cdot\beta}u_{\theta|\alpha} + v_{\alpha|\beta} + v_{\beta|\alpha}\\
2\bar{E}^{(2)}_{\alpha\beta} &= K^{\theta}_{\cdot\alpha}v_{\theta|\beta} + K^{\theta}_{\cdot\beta}v_{\theta|\alpha}\\
2\bar{E}^{(0)}_{\alpha 3} &= u_{3|\alpha} + v_{\alpha} \qquad 2\bar{E}^{(1)}_{\alpha 3} = v_{3,\alpha} \qquad \bar{E}^{(0)}_{33} = v_3.
\end{aligned} \tag{6}$$

The superscripts indicate the dependence on the thickness coordinate ξ^3: $\bar{E}^{(0)}$ is independent of ξ^3, $\bar{E}^{(1)}$ varies linearly with ξ^3 and $\bar{E}^{(2)}$ varies quadratically, such that

$$\bar{E}_{ij} = \bar{E}^{(0)}_{ij} + \xi^3\bar{E}^{(1)}_{ij} + (\xi^3)^2\bar{E}^{(2)}_{ij}. \tag{7}$$

These expressions clearly separate the contributions of the mid-surface displacement $\mathbf{u}$ and the director variation $\mathbf{v}$, providing a systematic representation of membrane, bending, and transverse shear strains within the six-field shell formulation.

2.2.2. Five-parameter shell theory

In the five-parameter shell theory, the shell thickness is assumed to remain constant, while transverse shear deformation is still allowed. This assumption corresponds to enforcing $v_3 = 0$ which implies $\bar{E}^{(0)}_{33} = 0$ and $\bar{E}^{(1)}_{\alpha 3} = 0$.

Under these conditions, the kinematic description involves five independent fields: the three components of the mid-surface displacement vector $\mathbf{u}$ and the two components of the director variation vector $\mathbf{v}$, which represent the rotations of the director. The strain components preserve the structure of the Reissner–Mindlin formulation, except for the suppression of thickness stretching, and are expressed as

$$\begin{aligned}
2\bar{E}^{(0)}_{\alpha\beta} &= u_{\alpha|\beta} + u_{\beta|\alpha}\\
2\bar{E}^{(1)}_{\alpha\beta} &= K^{\theta}_{\cdot\alpha}u_{\theta|\beta} + K^{\theta}_{\cdot\beta}u_{\theta|\alpha} + v_{\alpha|\beta} + v_{\beta|\alpha}\\
2\bar{E}^{(2)}_{\alpha\beta} &= K^{\theta}_{\cdot\alpha}v_{\theta|\beta} + K^{\theta}_{\cdot\beta}v_{\theta|\alpha}\\
2\bar{E}^{(0)}_{\alpha 3} &= u_{3|\alpha} + v_{\alpha}.
\end{aligned} \tag{8}$$

Finally, the normal stress through the thickness is neglected, leading to a plane stress condition.

2.2.3. Sanders–Koiter theory

Here, the Sanders–Koiter shell theory is obtained as a limiting case of the five-parameter formulation by enforcing the Kirchhoff–Love hypotheses, which are valid for thin shells ($h/R \ll 1$). In this limit, transverse shear deformation and thickness stretching are neglected, resulting in membrane–bending kinematics without transverse shear or thickness stretching.

This reduction is achieved by imposing that the director remains normal to the deformed mid-surface. This assumption leads to

$$\bar{E}^{(0)}_{\alpha 3} = \frac{1}{2}(u_{3|\alpha} + v_{\alpha}) = 0 \qquad \Longrightarrow \qquad v_{\alpha} = -u_{3|\alpha}. \tag{9}$$

As a consequence, the five independent kinematic fields of the Reissner–Mindlin formulation are reduced to three mid-surface displacement components, since the director rotations are fully determined by the transverse displacement. The resulting strain–displacement relations retain only the mid-surface stretching strains and the changes of curvature. Neglecting higher-order terms in the thickness coordinate, the nonzero strain measures of the Sanders–Koiter theory are given by

$$\begin{aligned}
\gamma_{\alpha\beta} &= \frac{1}{2}\left(u_{\alpha|\beta} + u_{\beta|\alpha}\right)\\
\rho_{\alpha\beta} &= \Gamma^{\gamma}_{\alpha\beta}u_{3|\gamma} - u_{3|\alpha\beta} + \frac{1}{2}\left(K^{\sigma}_{\cdot\alpha}u_{\sigma|\beta} + K^{\sigma}_{\cdot\beta}u_{\sigma|\alpha}\right)
\end{aligned} \tag{10}$$

where $\varepsilon_{\alpha\beta}$ denotes the membrane strain tensor and $\rho_{\alpha\beta}$ represents the change of curvature tensor of the mid-surface, such that

$$\mathbf{E} = (\gamma_{\alpha\beta} + \xi^3\rho_{\alpha\beta})\mathbf{M}_{\alpha} \otimes \mathbf{M}_{\beta}. \tag{11}$$

2.3. Shell's energy

For elastic materials, the strain energy of the shell is computed as

$$U = \int_{\mathcal{V}} U_0(\mathbf{E})\,\mathrm{d}\mathcal{V} \tag{12}$$

where $\mathbf{E}$ denotes the Green–Lagrange strain tensor and $U_0(\mathbf{E})$ is the strain energy density function. For linear elastic materials, the energy function is given by

$$U_0(\mathbf{E}) = \frac{1}{2}\mathbf{E} : \mathbf{C} : \mathbf{E} \tag{13}$$

where $\mathbf{C}$ is the constitutive tensor for a Saint Venant–Kirchhoff material.

The kinetic energy is expressed as

$$\begin{aligned}
T &= \frac{1}{2}\int_{\mathcal{V}} \rho\dot{\mathbf{x}}\cdot\dot{\mathbf{x}}\,\mathrm{d}\mathcal{V}\\
&= \frac{1}{2}\iint_{\Omega}\int_{-h/2}^{h/2} \rho\left(\dot{u}^i\dot{u}_i + 2\xi^3\dot{u}^i\dot{v}_i + (\xi^3)^2\dot{v}^i\dot{v}_i\right)\sqrt{G}\,\mathrm{d}\xi^3\mathrm{d}\xi^1\mathrm{d}\xi^2
\end{aligned} \tag{14}$$

where ρ is the mass density per unit volume, and the kinematics is expressed in terms of the mid-surface displacement $\mathbf{u}$ and the director variation $\mathbf{v}$.

2.4. Displacement expansion

2.4.1. Index mapping

The methodology presented here starts from a fully coupled representation of the shell displacement field. However, for the purposes of this study, the displacement field is considered in a decoupled form, with separate expansions for the mid-surface displacements $\mathbf{u}$ and the director variation $\mathbf{v}$. In the present implementation, the formulation is kept in a coupled form, which can be advantageous if the displacement field is expanded in terms of vibration modes or reduced-order bases.

The displacement field is approximated by finite expansions

$$\mathbf{U}(\xi^1,\xi^2,\xi^3,t) = \sum_{r=1}^{N} A_r(t)\left(\mathbf{F}^r(\xi^1,\xi^2) + \xi^3\mathbf{G}^r(\xi^1,\xi^2)\right) \tag{15}$$

where each vector basis $\mathbf{F}_r$ and $\mathbf{G}_r$ has three components. In compact form, the expansions are

$$\begin{aligned}
\sum_{r=1}^{N} A_r(t)\,\mathbf{F}^r(\xi^1,\xi^2) &= \mathbf{u}(\xi^1,\xi^2,t)\\
\sum_{r=1}^{N} A_r(t)\,\mathbf{G}^r(\xi^1,\xi^2) &= \mathbf{v}(\xi^1,\xi^2,t)
\end{aligned} \tag{16}$$

where the same coefficients $A_r(t)$ would be used in the fully coupled form, and separate coefficients can be introduced in the decoupled case.

To make the association between basis functions and vector components, we introduce a mapping $r \longmapsto (k_r, i_r, j_r)$ with

- $k_r \in \{1,2,3,4,5,6\}$ identifies the displacement field associated with the basis function r: $k_r = 1,2,3$ correspond to the mid-surface displacement fields u_1, u_2, u_3 and $k_r = 4,5,6$ correspond to the director variation fields v_1, v_2, v_3;
- i_r and j_r index the one-dimensional shape functions $\phi_i^{(1)}(\xi^1)$ and $\phi_j^{(2)}(\xi^2)$.

Each basis function is therefore associated with a single displacement field, so that the shape functions are fully decoupled with respect to the six components of the displacement vector. Accordingly, the kth component of $\mathbf{F}^r$ and $\mathbf{G}^r$ is written as

$$F_k^r(\xi^1,\xi^2) = \delta_{k_r}^k \, \phi_{i_r}^{(1)}(\xi^1)\,\phi_{j_r}^{(2)}(\xi^2)$$
$$G_k^r(\xi^1,\xi^2) = \delta_{k_r}^k \, \phi_{i_r}^{(1)}(\xi^1)\,\phi_{j_r}^{(2)}(\xi^2) \tag{17}$$

where the corresponding vector fields are

$$\mathbf{F}^r = F_k^r \mathbf{M}^k$$
$$\mathbf{G}^r = G_k^r \mathbf{M}^{\tilde{k}} \qquad \tilde{k} = k-3 \text{ for } k = 4,5,6. \tag{18}$$

Here, $\delta_{k_r}^k$ is the Kronecker delta that enforces that each shape function acts only in its associated displacement field k_r.

Equivalently, one may introduce a multi-index notation (k,i,j) and write the expansions as sums over the admissible triples:

$$\mathbf{u}(\xi^1,\xi^2,t) = \sum_{(k,i,j)\in\mathcal{I}_u} B_{k,i,j}(t)\,\mathbf{M}^k \phi_i^{(1)}(\xi^1)\phi_j^{(2)}(\xi^2)$$
$$\mathbf{v}(\xi^1,\xi^2,t) = \sum_{(k,i,j)\in\mathcal{I}_v} C_{k,i,j}(t)\,\mathbf{M}^k \phi_i^{(1)}(\xi^1)\phi_j^{(2)}(\xi^2) \tag{19}$$

where $\mathcal{I}_u$ and $\mathcal{I}_v$ are the index sets of triples assigned to the $\mathbf{u}$ and $\mathbf{v}$ fields, respectively. This form makes explicit that each basis function is associated with a single vector component and a separable spatial shape.

The time-dependent coefficients $A_r(t)$ (or their equivalents $B_{k,i,j}(t)$ and $C_{k,i,j}(t)$) act as generalized coordinates for the system, governing the temporal evolution of the structural response. Their dynamics are obtained from the variational formulation, leading to a set of ordinary differential equations that capture the essential behavior of the original continuous model, as shown below.

Finally, the total number of generalized coordinates (degrees of freedom) can be expressed as

$$N = n_f\, n_1^f\, n_2^f \tag{20}$$

where the factor n_f accounts for the number of fields depending on the adopted theory, and n_1^f and n_2^f denote the number of shape functions along ξ^1 and ξ^2, respectively, for each displacement field. Although not all of these functions need to be retained for a given problem, the selection of the shape functions was guided by a convergence study, progressively increasing n_1^f and n_2^f until the results reached convergence.

2.4.2. Hierarchic trigonometric sets

The displacement expansions presented in the previous section require a set of suitable basis functions to approximate the surface fields $\mathbf{u}$ and $\mathbf{v}$. In this study, enriched cosine basis functions are employed, following the methodology proposed by [43]. This approach allows for the enforcement of boundary conditions in a straightforward manner while maintaining good convergence properties. Two sets of basis functions are considered: C^0 continuous and C^1 continuous. In the present work, the C^0 set is used for the in-plane and director components u_1, u_2, v_1, v_2, v_3, whereas the transverse displacement u_3 is represented using the C^1 set, which provides higher continuity suitable for bending behavior.

The enriched cosine functions for C^0 continuity are defined as

$$\phi_1 = \frac{1}{4}(3\xi+1)(\xi-1) \qquad \phi_2 = \frac{1}{4}(3\xi-1)(\xi+1)$$

$$\phi_j = \cos\frac{\pi}{2}(j-3)(\xi+1) - \phi_1 + (-1)^j\phi_2 \qquad \text{for } j = 3,4\ldots \tag{21}$$

Table 2
C^0 boundary conditions for in-plane and director displacement fields.

Boundary condition	$\xi=-1$	$\xi=1$
Free	full series retained	full series retained
Restrained	remove ϕ_1	remove ϕ_2

Table 3
C^1 boundary conditions for transverse displacement u_3.

Boundary condition	$\xi=-1$	$\xi=1$
Free	full series retained	full series retained
Pinned	remove ϕ_1	remove ϕ_2
Clamped	remove ϕ_1 and ϕ_3	remove ϕ_2 and ϕ_4
Rotation-restrained	remove ϕ_3	remove ϕ_4

These functions satisfy C^0 continuity and can be directly truncated or modified to impose the desired boundary conditions. Table 2 summarizes the treatment of restrained boundaries, where the corresponding ϕ_1 or ϕ_2 is removed at $\xi=-1$ or $\xi=1$. Here, each standard interval $\xi\in[-1,1]$ is mapped to the physical coordinate directions $\xi^\alpha\in[\xi_l^\alpha,\xi_r^\alpha]$ for $\alpha=1,2$ using a linear transformation:

$$\xi = \frac{2\xi^\alpha - (\xi_r^\alpha + \xi_l^\alpha)}{\xi_r^\alpha - \xi_l^\alpha}. \tag{22}$$

This linear mapping allows the shape functions, originally defined on the standard interval $[-1,1]$, to be consistently applied over a rectangular domain Ω, while correctly accounting for the boundary conditions imposed along the shell edges.

The transverse displacement u_3 requires C^1 continuity for accurate bending representation. The enriched cosine set for C^1 reads

$$\phi_1 = -\frac{1}{16}(3\xi+1)(5\xi+7)(\xi-7)^2 \qquad \phi_2 = -\frac{L}{32}(\xi+1)(5\xi+1)(\xi-1)^2$$
$$\phi_3 = -\frac{1}{16}(3\xi-1)(5\xi-7)(\xi+7)^2 \qquad \phi_4 = \frac{L}{32}(\xi-1)(5\xi-1)(\xi+1)^2$$
$$\phi_j = \cos\frac{\pi}{2}(j-5)(\xi+1) - \phi_1 + (-1)^j\phi_3 \qquad \text{for } j = 5,6\ldots \tag{23}$$

where $L = \xi_r^\alpha - \xi_l^\alpha$. The associated boundary conditions are summarized in Table 3. Clamped, pinned, and rotation-restrained boundaries are enforced at the domain endpoints by removing specific functions, as indicated.

Expansions based on orthogonal polynomials, such as Legendre polynomials, are known to offer strong algebraic orthogonality and are attractive in Ritz formulations defined on standard domains. In contrast, enriched trigonometric expansions retain spectral-like convergence, naturally accommodate periodicity, and allow for the straightforward enforcement of boundary conditions through selective removal of basis functions. The enriched cosine series is obtained by expanding a modified cosine series, including an auxiliary polynomial to enforce continuity of the periodic extension and of its derivatives up to a prescribed order. This modification suppresses the Gibbs phenomenon associated with standard Fourier expansions and yields a faster decay of the coefficients. Further details can be found in [43].

2.4.3. Shape functions on a periodic coordinate

For shells where the curvilinear coordinate follows a closed loop with periodic continuity, such that the start and end points coincide, the shape functions along the coordinate ξ^θ ($\theta=1$, $\theta=2$, or both, as in the case of a torus) can be represented as a Fourier series. The functions are defined on the interval $[\xi_l^\theta,\xi_r^\theta]$, which is periodic, and mapped to $[0,2\pi]$ via

$$\xi = 2\pi\frac{\xi^\theta - \xi_l^\theta}{\xi_r^\theta - \xi_l^\theta}. \tag{24}$$

The shape functions $\phi_j(\xi^\theta)$ are then defined as

$$\phi_j(\xi) = \begin{cases} \cos \dfrac{j}{2}\xi & j = 0, 2, 4 \ldots \\ \sin \dfrac{j+1}{2}\xi & j = 1, 3, 5 \ldots \end{cases} \tag{25}$$

so that each even index corresponds to a cosine term and each odd index corresponds to a sine term. It should be noted that the shell does not need to be axisymmetric. The inclusion of both sine and cosine terms in the Fourier series allows the representation of asymmetric displacement patterns along the curvilinear closed-loop coordinate.

2.5. Büchter–Ramm–Roehl shell theory

Six-parameter shell theories extend classical formulations by introducing an independent thickness stretch, thereby allowing the description of shell kinematics in the presence of large displacements and rotations. This extension represents a step back toward a three-dimensional continuum description when compared to classical three-parameter theories based on the Kirchhoff–Love hypothesis, as well as five-parameter formulations employing Reissner–Mindlin kinematics. In these lower-order theories, it is standard practice to condense the three-dimensional constitutive relations by enforcing a vanishing stress in the thickness direction, which renders the thickness strain a dependent variable. While such condensation procedures are adequate for many applications, they become questionable when stresses and strains in the thickness direction play a non-negligible role [36].

However, although the six-parameter formulation provides a richer kinematic description, it does not necessarily yield accurate results. The assumption of a linear displacement variation across the thickness leads to a constant thickness strain, which, when combined with a constant normal stress assumption, requires an additional condensation of the bending part of the constitutive law. If this condensation is not performed consistently, even linear analyses may exhibit relative errors of order ν^2. As a result, six-parameter shell theories may exhibit numerical pathologies such as volumetric and thickness-related locking, including Poisson locking, which manifests as an artificially stiff structural response. These deficiencies are particularly pronounced in bending-dominated problems and in the analysis of nearly incompressible materials [10,36].

To overcome these limitations, the Büchter–Ramm–Roehl shell theory [36] is employed. Within this framework, the strain field is enriched by introducing an independent assumed strain component in addition to the compatible strain derived from the displacement field. Consequently, the total strain is decomposed into a compatible part and an enhanced part. Starting from the Hu–Washizu functional, the governing equations are derived as

$$U_{HW}(\mathbf{U}, \mathbf{E}, \mathbf{S}) = \int_{\mathcal{V}} \left[U_0(\mathbf{E}) - \mathbf{S} : \left(\mathbf{E} - \mathbf{E}^{\mathrm{comp}}(\mathbf{U}) \right) \right] \mathrm{d}\mathcal{V} \tag{26}$$

where $\mathbf{U}$ denotes the displacement field, $\mathbf{E}$ the independent strain field, and $\mathbf{S}$ the corresponding stress field. Following the seven-parameter shell theory proposed by [36], the total strain tensor is defined as

$$\mathbf{E} = \mathbf{E}^{\mathrm{comp}}(\mathbf{U}) + \tilde{\varepsilon} \tag{27}$$

where $\mathbf{E}^{\mathrm{comp}}(\mathbf{U})$ denotes the compatible strain tensor associated with the displacement field $\mathbf{U}$, corresponding to the Green–Lagrange strain tensor, whose components are given in (6). The term $\tilde{\varepsilon}$ represents the enhanced assumed strain field.

The enhanced strain field

$$\tilde{\varepsilon} = \tilde{\varepsilon}_{33}\, \mathbf{M}^3 \otimes \mathbf{M}^3 \tag{28}$$

is introduced exclusively in the thickness strain component, with the corresponding non-vanishing component defined as

$$\tilde{\varepsilon}_{33} = \xi^3\, \mu(\xi^1, \xi^2) \tag{29}$$

where $\mu(\xi^1, \xi^2)$ is an independent scalar field defined on the shell mid-surface. The introduction of this additional field increases the number of parameters from six to seven, allowing for a more flexible representation of the through-thickness deformation and contributing to the alleviation of thickness-related locking effects.

With the introduction of an independent enhanced strain field, a purely displacement-based energy functional is no longer adequate. Substituting the strain decomposition from (27) into the Hu–Washizu functional (26) and eliminating the independent strain field yields the following mixed formulation:

$$\tilde{U}(\mathbf{U}, \tilde{\varepsilon}, \mathbf{S}) = \int_{\mathcal{V}} \left[U_0(\mathbf{E}(\mathbf{U}) + \tilde{\varepsilon}) - \mathbf{S} : \tilde{\varepsilon} \right] \mathrm{d}\mathcal{V} \tag{30}$$

where $\mathbf{U}$, $\tilde{\varepsilon}$, and $\mathbf{S}$ denote the independent displacement, enhanced strain and stress fields, respectively.

This mixed variational principle enforces energetic consistency between the strain derived from the displacement field and the independent enhanced strain field in a weak sense. The energetic interaction between the enhanced strain field and the stress field is governed by an orthogonality condition, which is enforced through an appropriate choice of the enhanced strain approximation. Since only the thickness stretching component of the enhanced assumed strain is nonzero, the internal work contribution associated with the enhanced strain reduces to

$$\int_{\mathcal{V}} \tilde{\varepsilon} : \mathbf{S}\, \mathrm{d}\mathcal{V} = \int_{\mathcal{V}} S^{33}\, \tilde{\varepsilon}_{33}\, \mathrm{d}\mathcal{V} = \int_{\mathcal{V}} S^{33} \xi^3\, \mu(\xi^1, \xi^2)\, \mathrm{d}\mathcal{V}. \tag{31}$$

Assuming a constant approximation for the thickness stress component S^{33} through the shell thickness, the energetic orthogonality condition simplifies to

$$\int_{\mathcal{V}} \xi^3\, \mu(\xi^1, \xi^2)\, \mathrm{d}\mathcal{V} = 0. \tag{32}$$

To satisfy this requirement, the scalar field $\mu(\xi^1, \xi^2)$ is approximated by a finite expansion of orthogonal basis functions,

$$\mu(\xi^1, \xi^2) = \sum_{s=1}^{M} \alpha_s\, \psi_{i_s}(\xi^1)\, \psi_{j_s}(\xi^2) \tag{33}$$

where a mapping $s \longmapsto (i_s, j_s)$ is introduced and M denotes the total number of internal variables. The functions ψ_{i_s} and ψ_{j_s} are chosen as Legendre polynomials due to their orthogonality properties, which ensure energetic orthogonality of the enhanced strain modes with respect to the assumed constant stress field. For periodic coordinates, a Fourier series expansion is adopted, naturally satisfying periodicity and preserving the orthogonality of the basis functions.

As a consequence, the enhanced assumed strain does not contribute spurious internal work, effectively alleviating volumetric and thickness-related locking phenomena. The internal energy of the shell can therefore be written as

$$\tilde{U}(\mathbf{U}, \mu) = \int_{\mathcal{V}} U_0(\mathbf{E}(\mathbf{U}) + \tilde{\varepsilon})\, \mathrm{d}\mathcal{V}. \tag{34}$$

If the enhanced strain field vanishes, i.e. $\mu(\xi^1, \xi^2) = 0$, the enhanced strain contribution $\tilde{\varepsilon}$ disappears, the mixed functional reduces to the original energy functional (12), and the formulation recovers the standard six-parameter shell theory.

While the assumed strain defined in Eqs. (28)–(29) mitigates locking phenomena, the fidelity of the through-thickness strain description is inherently limited by the order of the adopted kinematic expansion. Previous higher-order formulations have demonstrated that enriched thickness representations can significantly improve the prediction of transverse normal deformation fields [44,45].

2.6. Constitutive tensor

For a linear elastic material, the constitutive behavior is described by a fourth-order tensor. In curvilinear coordinates, this tensor can be written as

$$\mathbf{C} = \bar{C}^{ijkl}\, \bar{\mathbf{M}}_i \otimes \bar{\mathbf{M}}_j \otimes \bar{\mathbf{M}}_k \otimes \bar{\mathbf{M}}_l. \tag{35}$$

The strain energy density can be expressed, using vectorization, as

$$U_0 = \frac{1}{2}\{\bar{E}\}^T[\bar{C}]\{\bar{E}\} \tag{36}$$

allowing the fourth-order tensor to be represented as a matrix suitable for numerical computations. The components $\bar{E}_{ij}$ form a 3×3 matrix, which is reshaped into a 9×1 column vector $\{\bar{E}\}$ through vectorization. Similarly, the components of the fourth-order constitutive tensor $\bar{C}^{ijkl}$, originally forming a $3\times3\times3\times3$ array, are mapped into a 9×9 matrix $[\bar{C}]$ by combining pairs of indices: (i, j) from the first two indices are mapped to the row index, and (k, l) from the last two indices are mapped to the column index.

It is convenient to express the constitutive tensor in an orthonormal basis $\tilde{\mathbf{e}}_i$ where the tensor takes the simple form

$$\mathbf{C} = \hat{C}_{ijkl}\, \hat{\mathbf{e}}_i \otimes \hat{\mathbf{e}}_j \otimes \hat{\mathbf{e}}_k \otimes \hat{\mathbf{e}}_l. \tag{37}$$

The orthonormal basis offers not only a convenient framework for computations but also the natural reference system in which material parameters are typically defined. A practical orthonormal triad

$$\hat{\mathbf{e}}_1 = \frac{\bar{\mathbf{M}}_1}{|\bar{\mathbf{M}}_1|} \qquad \hat{\mathbf{e}}_2 = \frac{\bar{\mathbf{M}}^2}{|\bar{\mathbf{M}}^2|} \qquad \hat{\mathbf{e}}_3 = \bar{\mathbf{M}}_3 \tag{38}$$

can be constructed by selecting two vectors tangent to the mid-surface and one vector aligned with the surface normal. In this construction, $\hat{\mathbf{e}}_1$ and $\hat{\mathbf{e}}_2$ span the tangent plane of the mid-surface, whereas $\hat{\mathbf{e}}_3$ coincides with the outward unit normal. Aligning the orthonormal basis with the local tangents is particularly advantageous when material properties vary through the thickness (e.g. fiber-reinforced shells, orthotropic laminates, or functionally graded materials) because it simplifies both the constitutive description and the projection of material parameters onto the mid-surface.

Let $R_{ij} = \hat{\mathbf{e}}_i \cdot \bar{\mathbf{M}}^j$ denote the components of the contravariant basis vectors in the orthonormal frame. The strain tensor in the orthonormal basis is

$$\mathbf{E} = \hat{E}_{kl}\hat{\mathbf{e}}_k \otimes \hat{\mathbf{e}}_l \qquad \hat{E}_{kl} = R_{ki}\bar{E}_{ij}R_{lj} \tag{39}$$

or, in vectorized form,

$$\{\hat{E}\} = ([R] \otimes [R])\{\bar{E}\} \tag{40}$$

so the strain energy density can also be expressed in the material frame as

$$U_0 = \frac{1}{2}\{\hat{E}\}^T[\hat{C}]\{\hat{E}\}. \tag{41}$$

Using the Voigt notation the symmetric strain tensor can be vectorized in a compact form

$$\{\hat{E}\}_{\text{Voigt}} = [P]\{\hat{E}\} \qquad \{\hat{E}\} = [P^+]\{\hat{E}\}_{\text{Voigt}}, \tag{42}$$

that eliminates redundant components and rescales the shear terms, with

$$[P] = \begin{bmatrix} 1&0&0&0&0&0&0&0&0\\ 0&0&0&0&1&0&0&0&0\\ 0&0&0&0&0&0&0&0&1\\ 0&0&0&0&0&1&0&1&0\\ 0&0&1&0&0&0&1&0&0\\ 0&1&0&1&0&0&0&0&0 \end{bmatrix}$$

$$[P^+] = \begin{bmatrix} 1&0&0&0&0&0\\ 0&0&0&0&0&\frac{1}{2}\\ 0&0&0&0&\frac{1}{2}&0\\ 0&0&0&0&0&\frac{1}{2}\\ 0&1&0&0&0&0\\ 0&0&0&\frac{1}{2}&0&0\\ 0&0&0&0&\frac{1}{2}&0\\ 0&0&0&\frac{1}{2}&0&0\\ 0&0&1&0&0&0 \end{bmatrix}. \tag{43}$$

Here, the operators $\{\cdot\}_{\text{Voigt}}$ or $[\cdot]_{\text{Voigt}}$ indicate that the tensors are written in Voigt notation: symmetric second-order tensors (strain or stress) are represented as 6×1 vectors, while the fourth-order constitutive tensor is represented as a 6×6 matrix.

Substituting (40) and (42) into (41), the strain energy density can be expressed as

$$U_0 = \frac{1}{2}\{\bar{E}\}^T_{\text{Voigt}}\left([T]^T[\hat{C}]_{\text{Voigt}}[T]\right)\{\bar{E}\}_{\text{Voigt}} \tag{44}$$

where $[\hat{C}]_{\text{Voigt}}$ is the constitutive matrix defined in the material frame and using Voigt notation, and $\{\bar{E}\}_{\text{Voigt}}$ is the strain vector evaluated in the shell frame using Voigt notation. The transformation matrix $[T]$ maps quantities between these two frames, ensuring consistency between the material law and the shell formulation:

$$[T] = [P]([R] \otimes [R])[P^+]. \tag{45}$$

Although (44) can accommodate general types of linear elastic behavior for shell analysis, in this work only a few representative cases are illustrated.

Here, the material is intrinsically orthotropic and is described in a rotated global reference frame aligned with an in-plane rotation of the fiber directions. The resulting constitutive matrix

$$[\hat{C}]_{\text{Voigt}} = \begin{bmatrix} \hat{C}_{11} & \hat{C}_{12} & \hat{C}_{13} & 0 & 0 & \hat{C}_{16}\\ \hat{C}_{12} & \hat{C}_{22} & \hat{C}_{23} & 0 & 0 & \hat{C}_{26}\\ \hat{C}_{13} & \hat{C}_{23} & \hat{C}_{33} & 0 & 0 & 0\\ 0 & 0 & 0 & \hat{C}_{44}\kappa_2^2 & \hat{C}_{45}\kappa_3^2 & 0\\ 0 & 0 & 0 & \hat{C}_{45}\kappa_3^2 & \hat{C}_{55}\kappa_1^2 & 0\\ \hat{C}_{16} & \hat{C}_{26} & 0 & 0 & 0 & \hat{C}_{66} \end{bmatrix} \tag{46}$$

includes shear correction factors arising from the adopted plate/shell kinematic assumptions. The coefficients C_{ij} are functions of the nine independent elastic constants of the orthotropic material (E_1, E_2, E_3, G_{12}, G_{13}, G_{23}, ν_{12}, ν_{13}, ν_{23}) as well as of the rotation angle α with respect to the $\hat{\mathbf{e}}_3$ axis. The shear correction factors κ_1 and κ_2 are determined by enforcing the static cylindrical bending condition about the $\hat{\mathbf{e}}_1$ and $\hat{\mathbf{e}}_2$ axes, following the procedure proposed in [46]. This approach relies on the strain energy equivalence method, ensuring that the SCFs accurately reflect the specific stacking sequence and material anisotropy of the laminate. By explicitly accounting for the extensional, coupling, and bending stiffnesses, these refined factors overcome the limitations of the traditional $5/6$ constant, especially for unsymmetric and angle-ply configurations. Furthermore, this formulation remains valid for general doubly curved shells, as the equilibrium equations under the assumed bending conditions converge to the same functional form as plate theories [46]. In accordance with the same reference, the coupling factor is defined as $\kappa_3^2 = \kappa_1\kappa_2$.

For functionally graded materials (FGM), the elastic properties (E, ν, ρ) vary spatially according to the base material properties (E_A, ν_A, ρ_A) and (E_B, ν_B, ρ_B) and a material distribution law $V_f(\xi^3)$ representing the volume fraction of one constituent. If the material is orthotropic and laminated, each layer possesses its own orthotropic properties and orientation. The constitutive behavior of the laminate is obtained by assembling the contributions of individual layers, typically using classical laminate theory. The overall laminate stiffness is then computed by integrating the layer properties through the thickness, resulting in an effective constitutive matrix that captures both the orthotropy of each layer and the stacking sequence of the laminate.

3. Ritz approximation

A finite-dimensional approximation of the shell is obtained by enforcing stationarity of the energy functional

$$\mathscr{L}[\mathbf{U},\mu] = \int_{t_0}^{t_1} \left(T[\dot{\mathbf{U}}] - \tilde{U}[\mathbf{U},\mu]\right) \mathrm{d}t \tag{47}$$

with U and T defined in (12)–(14) and (34).

Introducing the Ritz expansions (15) for the displacement field and for the enhanced strain field, and requiring $\delta\mathscr{L} = 0$ for arbitrary variations of the generalized coordinates, leads to the discrete equations of motion

$$[M]\{\ddot{x}(t)\} + [K]\{x(t)\} = \{0\} \tag{48}$$

where the vector of generalized coordinates is partitioned as

$$\{x\} = \begin{Bmatrix} \{A\} \\ \{\alpha\} \end{Bmatrix} \tag{49}$$

with $\{A\} = \{A_1, \dots A_N\}$ denoting the displacement-related degrees of freedom and $\{\alpha\} = \{\alpha_1, \dots \alpha_M\}$ representing the internal EAS variables. The stiffness matrix assumes the block structure

$$[K] = \begin{bmatrix} [K_{AA}] & [K_{A\alpha}] \\ [K_{\alpha A}] & [K_{\alpha\alpha}] \end{bmatrix} \tag{50}$$

while the mass matrix

$$[M] = \begin{bmatrix} [M_{AA}] & [0] \\ [0] & [0] \end{bmatrix} \tag{51}$$

involves only the displacement degrees of freedom.

Because the enhanced strain parameters $\{\alpha\}$ are internal variables without associated inertia, they can be eliminated by means of static condensation as follows. Solving the algebraic relation

$$[K_{\alpha\alpha}]\{\alpha\} = -[K_{\alpha A}]\{A\} \tag{52}$$

and substituting into the equilibrium equations yields the condensed system

$$[M_{AA}]\{\ddot{A}(t)\} + [K]^{\mathrm{cond}}\{A(t)\} = \{0\} \tag{53}$$

where the condensed stiffness matrix

$$[K]^{\mathrm{cond}} = [K_{AA}] - [K_{A\alpha}][K_{\alpha\alpha}]^{-1}[K_{\alpha A}] \tag{54}$$

accounts for the effect of the enhanced assumed strain modes while preserving the original displacement-based degrees of freedom. Essential boundary conditions on $\mathbf{u}$ and $\mathbf{v}$ are enforced *a priori* by selecting the shape functions (18) to vanish along the prescribed edges of Ω.

For free-vibration analysis, the generalized coordinates are assumed to vary harmonically, $A_r(t) = \Phi_r e^{\mathrm{i}\omega t}$, reducing (53) to the eigenvalue problem

$$\left([K]^{\mathrm{cond}} - \omega^2[M_{AA}]\right)\{\Phi\} = \{0\} \tag{55}$$

whose solutions define the natural frequencies and mode shapes of the shell.

Compared to other numerical approaches, such as finite element or isogeometric methods, the Ritz methodology provides a global approximation of the solution fields, typically achieving high accuracy with a significantly lower number of degrees of freedom. This efficiency is particularly advantageous for nonlinear vibration analysis, where computational costs are highly sensitive to the size of the global system. Furthermore, while most traditional implementations of the Ritz method are case-dependent, often restricted to specific geometries due to the complexity of manual analytical derivations, the proposed framework overcomes these limitations by integrating symbolic computation for the automatic evaluation of shell parameters directly from the position vector. This ensures a unified and versatile approach that is not confined to predefined shapes, offering a robust alternative to the geometry-specific models typically found in the literature. Finally, boundary conditions can be enforced in a straightforward manner through the appropriate selection of enriched basis functions, ensuring both flexibility and numerical robustness.

4. Results

4.1. Computational aspects

The numerical results presented in this section were obtained using the ShellPy library, whose computational framework and underlying theoretical formulation were detailed in the previous sections. ShellPy is a Python library developed for the analysis of shell structures based on variational formulations. The library combines symbolic and numerical capabilities through the use of SymPy and NumPy, enabling the automatic determination of the geometric properties of the shell middle surface directly from the definition of the position vector.

The geometric description includes the computation of surface metrics, curvature measures, and thickness-related quantities, allowing the formulation to be applied to general shell geometries without requiring explicit analytical expressions for these quantities. The displacement fields can be set using different types of expansions, including trigonometric series, polynomial series, and eigenfunctions of beam vibration problems. This flexibility allows the consideration of a wide range of boundary conditions in a unified framework, making the library suitable for the analysis of shells with distinct support configurations.

ShellPy is designed to handle materials of different natures. Currently, the library includes implementations for isotropic materials, functionally graded materials, and orthotropic laminated composites. This enables the analysis of both homogeneous and heterogeneous shell structures, including laminated configurations with arbitrary stacking sequences. The integration of the energy functionals is performed numerically over the rectangular parametric domain Ω of the middle surface and through the thickness direction. This approach accommodates variable thickness distributions and spatial variations of material properties.

The code architecture was conceived to be modular and extensible, allowing straightforward implementation of new material models, kinematic assumptions, numerical integration schemes, and solution strategies. As a result, ShellPy provides a flexible and expandable framework for research and development in shell analysis.

Although the present study is restricted to single-patch geometries defined on a square parametric domain, the formulation is naturally suited to multi-patch extensions. Since the displacement fields are defined on parametric domains and boundary conditions are enforced by basis-function manipulation, standard multi-patch coupling strategies based on strong or weak continuity constraints can be incorporated without conceptual difficulty.

4.2. Numerical examples

All Ritz models associated with the numerical examples investigated in this work, including geometry definitions, material parameters, boundary conditions, and numerical settings, are made publicly available in the ShellPy repository [38], ensuring full reproducibility of the presented results. For validation purposes, finite element models were developed in the commercial software Ansys. The scripts used for the automatic generation of the corresponding finite element models, including geometry definition, mesh generation, and material properties, are also provided within the ShellPy repository.

4.2.1. Free vibration of functionally graded shells

Here, the free vibration behavior of simply supported moderately thick shells made of FGM is investigated for different curvature configurations. The objective is to assess the accuracy of the considered shell theories in predicting the vibration response of shells with varying curvature.

All shell edges are assumed to be simply supported, and the shell is composed of a mixture of metal and ceramic constituents whose volume fractions vary continuously through the thickness direction. The simply supported boundary conditions are expressed as $u_1 = u_3 = 0$ at $\xi^2 = 0, b$ and $u_2 = u_3 = 0$ at $\xi^1 = 0, a$. The material constituents considered in the present study are aluminum as the metal phase and alumina as the ceramic phase. The material properties of aluminum are $E_M = 70 \times 10^9$ N/m^2, $\nu_M = 0.3$ and $\rho_M = 2702$ kg/m^3. The properties of alumina are $E_C = 380 \times 10^9$ N/m^2, $\nu_C = 0.3$ and $\rho_C = 3800$ kg/m^3.

The shell middle surface is described using a Cartesian parametrization, which allows plates and doubly curved shells to be analyzed within a unified framework. The position vector of the middle surface is given by

$$\mathbf{R} = \xi^1 \mathbf{e}_1 + \xi^2 \mathbf{e}_2 + \left[\frac{1}{2R_x} \left(\xi^1 - \frac{a}{2} \right)^2 + \frac{1}{2R_y} \left(\xi^2 - \frac{b}{2} \right)^2 \right] \mathbf{e}_3 \tag{56}$$

where $0 \le \xi^1 \le a$ and $0 \le \xi^2 \le b$. The quantities a and b denote the in-plane dimensions of the shell, R_x and R_y are the principal radii of curvature along the ξ^1 and ξ^2 directions. A square planform is adopted with $a/b = 1$, and the shell thickness is taken as $h = a/10$. By varying the curvature ratios a/R_x and b/R_y, different shell geometries are obtained, including flat plates, cylindrical, spherical, and hyperbolic shells.

The effective material properties

$$E(\xi^3) = E_M + (E_C - E_M) V_f \qquad \rho(\xi^3) = \rho_M + (\rho_C - \rho_M) V_f \qquad \nu(\xi^3) = \nu_0 \tag{57}$$

of the functionally graded shell are assumed to vary only along the thickness coordinate ξ^3, according to a rule of mixtures, where V_f denotes the volume fraction and ν_0 is assumed to be constant for both constituents. The variation of the volume fraction through the thickness

$$V_f = \left(\frac{1}{2} + \frac{\xi^3}{h} \right)^p \tag{58}$$

is described by a power-law distribution, in which p is the power-law index controlling the material gradation. If $p = 0$, the shell is fully ceramic, whereas increasing values of p correspond to a higher metal content near the lower surface. All obtained results correspond to $p = 4$.

To assess the influence of the kinematic assumptions, the vibration responses are computed using shell theories with 5, 6, and 7 parameters. The results are compared with three-dimensional finite element solutions, as well as with reference solutions available in the literature. Table 4 presents these comparisons in terms of the non-dimensional frequency parameter $\Omega = \omega h \sqrt{\rho_C / E_C}$.

The three-dimensional finite element analysis was carried out using the commercial software Ansys. The shell was discretized with SOLID186 elements, employing a structured mesh of $50 \times 50 \times 10$ elements along the ξ^1, ξ^2, ξ^3 directions. Each layer through the thickness was assigned material properties according to the local value of the thickness coordinate ξ^3, following the prescribed functional gradation law. In order to properly enforce the simply supported boundary conditions, the nodal coordinate systems at the shell edges were rotated to align with the local tangential and normal directions. Additional kinematic constraints were imposed at the boundary nodes to ensure that the shell motion at the edges follows the shell director vector. This procedure guarantees a kinematically consistent edge behavior and helps to mitigate artificial stress concentrations that may arise from an improper enforcement of boundary conditions in three-dimensional finite element models. For this benchmark, 15 enriched trigonometric trial functions are retained, leading to $N = 1125$ degrees of freedom for the five-parameter theory and $N = 1350$ for the six- and seven-parameter theories. In contrast, the three-dimensional finite element model requires $314,559$ degrees of freedom to achieve comparable accuracy. Although the six- and seven-parameter theories involve a higher number of unknowns than the five-parameter model, no further increase in the global system size is observed when moving from six to seven parameters, as the additional thickness-stretching terms are handled via static condensation. These results highlight the computational advantage of the present Ritz-based approach, which provides accurate vibration characteristics using several orders of magnitude fewer degrees of freedom than the high-fidelity 3D finite element discretization.

The results show that the five-parameter shell theory systematically underestimates the natural frequencies, whereas the six-parameter formulation tends to overestimate them, especially in shells with lower curvature. In contrast, the seven-parameter formulation provides consistently accurate predictions for all curvature configurations considered, with relative discrepancies remaining below 1%, demonstrating its robustness with respect to both positive and negative Gaussian curvature. As the curvature increases, a clear stiffening effect is observed, leading to higher natural frequencies for spherical and cylindrical shells when compared to flat plates. Conversely, hyperbolic shells exhibit reduced stiffness due to their negative Gaussian curvature. Additional comparisons with the results reported by [47] further confirm the accuracy and robustness of the proposed seven-parameter formulation.

Fig. 2 illustrates the corresponding fundamental mode shapes obtained with the present formulation and the finite element model, highlighting the correct reproduction of the number of half-waves, modal symmetries, and locations of maximum transverse displacement for all curvature configurations.

4.2.2. Free vibration of an isotropic simply supported cylindrical shell

Now, the free vibration behavior of a simply supported cylindrical shell is investigated in order to verify the accuracy of the present seven-parameter shell formulation for different vibration modes. Particular attention is given to modes characterized by different dominant displacement fields, including transverse, in-plane, shear-related, and thickness-related deformations.

The cylindrical shell has radius $R = 0.15$ m, length $L = 0.52$ m, thickness $h = 0.03$ m. The material is assumed to be homogeneous and isotropic with $E = 198 \times 10^9$ Pa, $\nu = 0.3$ and $\rho = 7800$ kg/m^3. The geometry is described by the parametrization

$$\mathbf{R} = R \cos \xi^2 \mathbf{e}_1 + R \sin \xi^2 \mathbf{e}_2 + \xi^1 \mathbf{e}_3 \tag{59}$$

with $0 \le \xi^1 \le L$ and $0 \le \xi^2 \le 2\pi$. The directions ξ^1 and ξ^2 stand for the axial and circumferential coordinates. Simply supported boundary conditions are imposed at the shell ends, i.e. $u_2 = u_3 = v_2 = v_3 = 0$ at $\xi^1 = 0, L$.

The numerical results obtained using the present seven-parameter formulation are compared with three-dimensional finite element solutions computed in Ansys. The cylindrical shell was discretized using SOLID186 elements, adopting a structured mesh composed of $40 \times 80 \times 4$ elements along the ξ^1, ξ^2, ξ^3 directions. This discretization was found to be sufficient to accurately capture the global vibration characteristics of the shell while maintaining a reasonable computational cost. In this case, 10 enriched trigonometric trial functions are used, yielding $N = 600$ degrees of freedom, against 255,664 in the finite element model. The natural frequencies comparison is carried

Table 4
Comparison of non-dimensional frequency parameters for shells with different curvatures using five-, six-, and seven-parameter shell theories. The following configurations are considered: plate ($R_y = 0$), spherical shell ($R_x = R_y$), hyperbolic shell ($R_x = -R_y$) and cylindrical shell ($R_y = 0$). The error represents the relative difference with respect to the finite element results.

Geo.	a/R_x	Ansys	5-parameter		6-parameter		7-parameter		[47]	
			Ω	err. (%)	Ω	err (%)	Ω	err. (%)	Ω	err. (%)
Plt.	0	0.03655	0.03540	−3.12	0.04046	10.70	0.03655	0.00	0.03811	4.28
Sph.	0.5	0.04613	0.04505	−2.35	0.04901	6.24	0.04603	−0.21	0.05034	9.12
Sph.	1.0	0.06594	0.06476	−1.79	0.06735	2.13	0.06584	−0.16	0.07453	13.02
Hyp.	0.5	0.03397	0.03291	−3.10	0.03771	11.03	0.03400	0.10	0.03716	9.41
Hyp.	1.0	0.02865	0.02768	−3.36	0.03182	11.08	0.02867	0.10	0.03469	21.10
Cyl.	0.5	0.03825	0.03714	−2.91	0.04186	9.43	0.03819	−0.16	0.04131	8.00
Cyl.	1.0	0.04408	0.04305	−2.34	0.04679	6.16	0.04401	−0.15	0.04905	11.28

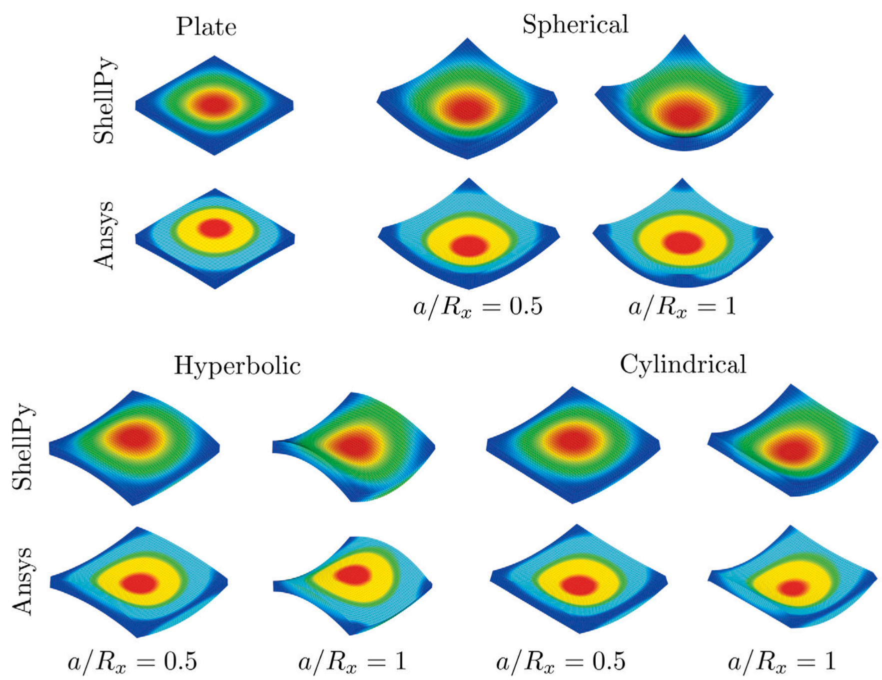

Fig. 2. First vibration mode shapes of simply supported functionally graded shells for different curvature configurations: plate, cylindrical, spherical, and hyperbolic shells. The results obtained with the present formulation are compared with finite element solutions, showing an excellent agreement in terms of modal shapes.

Table 5
Comparison of natural frequencies obtained from the present formulation, Ansys models, and the reference solution [44]. The mode numbers (m, n) denote the circumferential and axial wave numbers, respectively. The column "Dominant disp. field" indicates the displacement component (u_1, u_2, u_3, v_1, v_2, v_3) with the largest modal participation. The relative error is computed with respect to the finite element results.

(m,n)	Dominant	Ansys	Present		[44]	
	disp. field	Freq. (Hz)	Freq. (Hz)	Error (%)	Freq. (Hz)	Error (%)
$(1,2)$	u_3	1307.6	1306.8	−0.06	1305.9	−0.13
$(1,1)$	u_3	1758.8	1758.9	0.01	1756.7	−0.12
$(1,3)$	u_3	2559.8	2554.7	−0.20	2558.3	−0.06
$(1,0)$	u_3	4429.8	4429.8	0.00	4440.4	0.24
$(1,2)$	u_1	7626.9	7626.9	0.00	7646.0	0.25
$(1,2)$	u_2	13 181	13 187	0.05	13 163	−0.13
$(1,2)$	v_1	52 773	53 102	0.62	52 756	−0.03
$(1,2)$	v_2	54 200	54 724	0.97	54 248	0.09
$(1,2)$	v_3	98 792	107 668	8.98	97 299	−1.51

out for several vibration modes, each one associated with a distinct dominant displacement field, allowing a clear distinction between flexural, membrane, shear-related, and thickness-dominated vibration mechanisms. The results are summarized in Table 5.

Overall, an excellent agreement is observed between the present formulation and the finite element results for most vibration modes, particularly those dominated by transverse and in-plane displacement components. These modes primarily involve flexural and membrane-type deformations, which are well represented by the seven-parameter kinematic description. Some discrepancy arises for the mode dominated by thickness deformation, which strongly activates higher-order kinematics and through-thickness effects. This difference is attributed

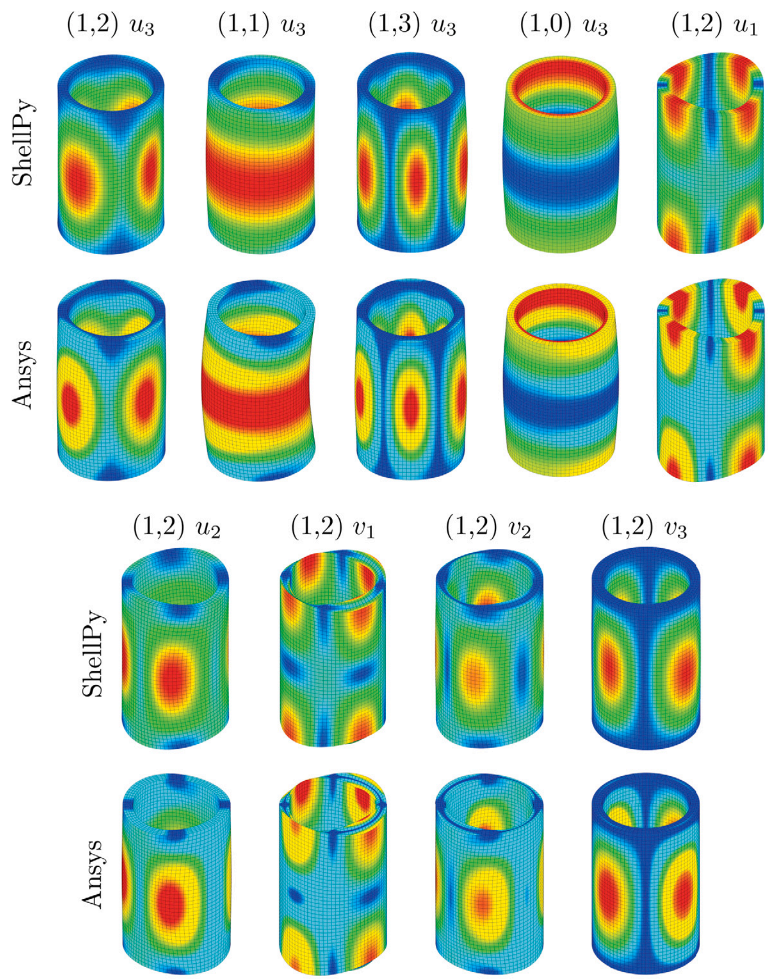

Fig. 3. Representative vibration mode shapes of the simply supported cylindrical shell associated with the modes listed in Table 5. The results obtained with the present formulation are compared with finite element solutions, showing an excellent agreement in terms of modal shapes.

to the distinct kinematic descriptions used for thickness deformation. While the present model employs a seven-parameter kinematic expansion, [44] adopts a more refined eight-parameter formulation, which provides an enhanced representation of through-thickness deformation effects. As a result, the reference solution achieves a closer agreement with the three-dimensional finite element results for this specific mode. Despite this limitation, the present formulation shows very good predictive capability for vibration modes dominated by transverse, in-plane, and shear-related displacement fields, providing a reliable compromise between accuracy and computational efficiency for practical engineering applications. The results indicate that, although a richer kinematic expansion may be required for modes strongly influenced by thickness deformation, the seven-parameter theory remains well suited for the analysis of a wide range of vibration modes in moderately thick shells.

Representative vibration mode shapes corresponding to selected modes listed in Table 5 are shown in Fig. 3. The comparison highlights the ability of the present formulation to accurately reproduce the global modal characteristics predicted by the three-dimensional finite element models.

4.2.3. Free vibration of laminated composite shells

In this section, the dynamic behavior of laminated composite shells is investigated using the seven-parameter shell theory to verify the influence of different lamination schemes on the vibration response. The accuracy of the formulation is assessed under conditions of strong material anisotropy and coupling effects induced by fiber orientation, focusing on shells composed of multiple orthotropic laminae arranged in various stacking sequences. Each lamina ply has thickness $h_{\text{ply}} = 0.13$ mm and the following material properties: $E_1 = 128$ GPa, $E_2 = E_3 = 11$ GPa, $G_{12} = G_{13} = 4.48$ GPa, $G_{23} = 1.53$ GPa, $\nu_{12} = \nu_{13} = 0.25$, $\nu_{23} = 0.45$, and $\rho = 1500$ kg/m^3.

The geometry is defined by a radius of curvature $R_b = 127.5$ mm and in-plane dimensions $a = 152.4$ mm and $b = 76.2$ mm along the ξ^1 and ξ^2 directions, respectively. The position vector of the mid-surface

$$\mathbf{R} = \xi^1 \mathbf{e}_1 + \xi^2 \mathbf{e}_2 + \sqrt{R_b^2 - \left(\xi^2 - \frac{b}{2}\right)^2}\,\mathbf{e}_3, \tag{60}$$

with $0 \le \xi^1 \le a$ and $0 \le \xi^2 \le b$, represents a shallow cylindrical panel with curvature along the ξ^2 direction while remaining flat along the ξ^1 direction. The panel is assumed to be cantilevered, with one edge fully clamped and the remaining edges free. The clamped boundary is located at $\xi^1 = 0$ where $u_1 = u_2 = u_3 = 0$, $v_1 = v_2 = v_3 = 0$ and $\partial u_3/\partial \xi^1 = 0$. None kinematic constraints are imposed along the other edges.

Table 6 presents a comparison of the natural frequencies obtained with the present formulation. The three-dimensional finite element models have structured meshes of 20 × 20 × 8 SOLID186 elements along the ξ^1, ξ^2 and ξ^3 directions. The element through the thickness direction ξ^3 represents an individual lamina, allowing for an actual layerwise modeling of the laminated composite. Here, 15 enriched trigonometric trial functions are retained, resulting in $N = 1350$ degrees of freedom for the seven-parameter theory, compared to 45,048 degrees of freedom in the finite element model. As verified through preliminary convergence analyses, the adopted mesh is sufficiently refined to ensure

Table 6
Comparison of natural frequencies of laminated composite cylindrical shell panels obtained from the present formulation, Ansys models, and the reference solution [14]. The shell is a clamped cylindrical panel. The stacking sequences are indicated using standard laminate notation, with the subscript s denoting symmetric laminates. The relative error is computed with respect to the finite element results.

Layup	Mode	Ansys	Present		[14]	
		Freq. (Hz)	Freq. (Hz)	Err. (%)	Freq. (Hz)	Err. (%)
	1	145.02	145.05	0.02	133.10	−8.22
	2	231.87	232.21	0.15	236.20	1.87
$[45/-45/-45/45]_s$	3	746.31	748.12	0.24	746.60	0.04
	4	789.03	790.12	0.14	758.80	−3.83
	5	1013.70	1017.71	0.40	1037.00	2.30
	1	165.61	164.12	−0.90	163.80	−1.09
	2	289.21	288.74	−0.16	269.50	−6.82
$[0/0/30/-30]_s$	3	586.09	584.85	−0.21	593.00	1.18
	4	713.80	704.30	−1.33	702.50	−1.58
	5	818.18	811.62	−0.80	824.80	0.81
	1	189.84	188.62	−0.64	190.80	0.51
	2	236.17	236.54	0.15	217.50	−7.91
$[0/45/-45/90]_s$	3	696.13	690.55	−0.80	695.50	−0.09
	4	788.65	787.17	−0.19	804.80	2.05
	5	959.75	959.12	−0.07	954.10	−0.59

mesh-independent results. The results in Table 6 demonstrate a close agreement between the present formulation and the finite element solutions obtained with Ansys for all lamination sequences and vibration modes analyzed, with relative differences remaining below 1% in most cases. This level of accuracy confirms the capability of the proposed model to correctly capture the dynamic behavior of laminated composite shells with different stacking sequences and strong material anisotropy. The comparison with the results reported by [14] shows larger discrepancies for some modes, likely due to differences in kinematic assumptions and numerical modeling strategies.

Fig. 4 illustrates the first vibration modes of the laminated cylindrical panel obtained with the present formulation and the three-dimensional finite element models. A good agreement is observed in terms of modal shapes, confirming that the proposed formulation accurately reproduces the dominant deformation patterns associated with lamination sequences.

4.2.4. *Free vibration of laminated orthotropic parabolic conoid shells*

This last example investigates the influence of boundary conditions on the free vibration characteristics of laminated orthotropic parabolic conoid shells. The objective is to assess the capability of the proposed Ritz formulation to accurately enforce different kinematic constraints in the presence of strong geometric coupling induced by double curvature and material anisotropy.

The parametrization

$$\mathbf{R} = \xi^1\mathbf{e}_1 + \xi^2\mathbf{e}_2 + f_1\left[1-\left(1-\frac{f_2}{f_1}\right)\frac{\xi^1}{a}\right]\left[1-\left(\frac{2\xi^2}{b}-1\right)^2\right]\mathbf{e}_3, \quad (61)$$

with $0 \le \xi^1 \le a$ and $0 \le \xi^2 \le b$, represents a doubly curved shell with opposite curvatures along the ξ^1 and ξ^2 directions, characteristic of parabolic conoidal surfaces. The geometric parameters are set as $a/b = 1$, $a/h = 100$, $a/f_2 = 5$ and $f_1/f_2 = 0.25$. The shell is modeled as a four-layer orthotropic laminate with stacking sequence [0/90/0/90]. Each lamina has uniform thickness $h/4$ and material defined by $E_{11}/E_{22} = 25$, $G_{12}/E_{22} = 0.5$, $\nu = 0.25$.

The considered boundary conditions include fully simply supported, fully clamped, mixed clamped–simply supported, and configurations involving free edges, allowing a comprehensive evaluation of the formulation under progressively relaxed kinematic constraints. All results are compared in Table 7 with three-dimensional finite element solutions by means of the non-dimensional frequency parameter $\omega a^2\sqrt{\rho/E_{22}h^2}$. The shell was discretized with 20-node quadratic hexahedral elements, employing a structured mesh of $20 \times 20 \times 4$ SHELL186 elements along the ξ^1, ξ^2 and ξ^3 directions. Using 15 enriched trigonometric trial functions, the proposed formulation requires only $N = 1350$ degrees of freedom in this case, in contrast to 21,147 in the finite element model.

Table 7
Comparison of the non-dimensional fundamental frequency $\bar{\omega}$ of laminated orthotropic parabolic conoid shells under different boundary conditions. The present results are compared with three-dimensional Ansys models and reference results [48]. The non-dimensional frequency is $\bar{\omega} = \omega a^2\sqrt{\rho/E_{22}h^2}$.

BC	Ansys	Present		[48]	
	Freq. ($\bar{\omega}$)	Freq. ($\bar{\omega}$)	Err. (%)	Freq. ($\bar{\omega}$)	Err. (%)
SSSS	53.3686	53.8813	0.96	53.0019	−0.69
CCCC	83.5349	83.5308	−0.00	87.9146	5.24
CCSS	62.3098	62.4212	0.18	64.8209	4.03
SSCC	77.7356	77.8550	0.15	81.7723	5.19
CSCS	64.0508	64.2769	0.35	65.8085	2.74
SCSC	61.3465	61.5271	0.29	62.1497	1.31
CCFF	46.8458	46.8967	0.11	50.8846	8.62
FFCC	59.3633	59.3711	0.01	60.7244	2.29
CFCF	7.9508	7.9551	0.05	8.0513	1.26
FCFC	27.6232	27.6366	0.05	28.4566	3.02

The results show a close agreement between the present formulation and Ansys models, with relative differences remaining below 1% for all assigned boundary conditions, demonstrating the ability of the proposed formulation to accurately enforce diverse kinematic constraints. Fully clamped configurations lead to the highest fundamental frequencies, reflecting the increased global stiffness imposed by the edge constraints, while configurations involving free edges exhibit a significant reduction in stiffness and, consequently, lower natural frequencies. The comparison with the reference results reported by [48] reveals a reasonable agreement for several cases, while discrepancies are observed depending on the imposed boundary conditions.

Fig. 5 illustrates representative fundamental vibration mode shapes of the parabolic conoid shell corresponding to the boundary condition configurations listed in Table 7. The qualitative agreement with the finite element solutions further confirms the robustness of the enriched cosine series in modeling diverse boundary conditions within the proposed seven-parameter framework.

It is worth noting that the percentage errors reported in Tables 4, 5, 6 and 7 are computed with respect to 3D finite element benchmarks, which serve as reference solutions. The observed discrepancies remain within the expected accuracy range for two-dimensional shell formulations, particularly for moderately thick configurations where higher-order kinematic assumptions are employed. These minor differences are primarily attributed to the inherent modeling gap between 3D elasticity and shell-theoretic assumptions. Moreover, consistent error

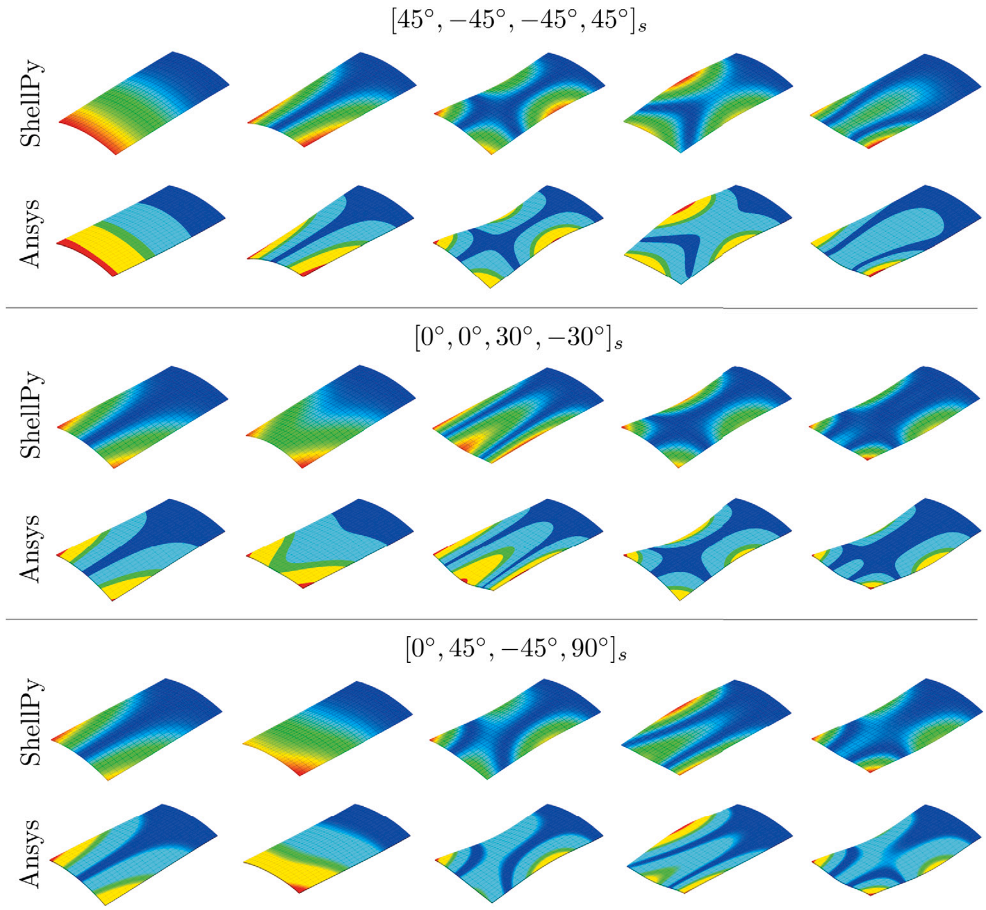

Fig. 4. Comparison of the vibration modes of the laminated cylindrical panel obtained with the present formulation and the three-dimensional finite element models for different stacking sequences.

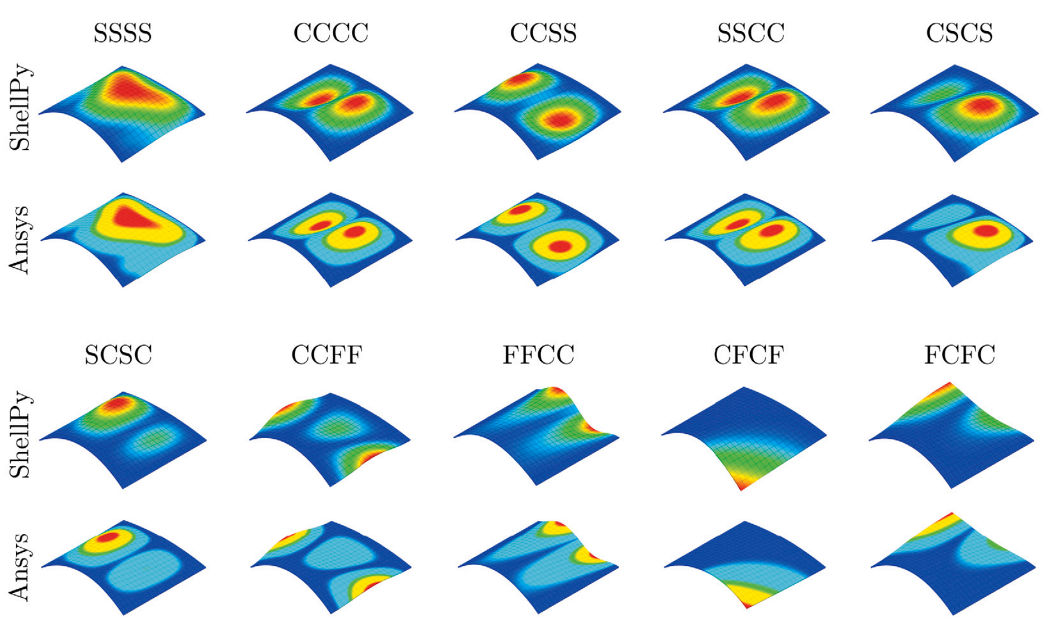

Fig. 5. Fundamental vibration mode shapes of the laminated orthotropic parabolic conoid shell corresponding to the boundary condition configurations reported in Table 7. The comparison shows a good qualitative agreement for all boundary conditions.

trends across different geometries and boundary conditions support the robustness of the proposed framework.

5. Conclusion

This work presented a unified Ritz-based framework for the free vibration analysis of shells, implemented within the ShellPy Python library. A key feature of the proposed approach is the seamless integration of symbolic and numerical computations, which enables the automatic evaluation of geometric quantities directly from the shell position vector. This strategy allows the analysis of a broad class of shell geometries, without requiring case-specific analytical derivations.

The formulation employs hierarchical sets of enriched trigonometric basis functions, which proved effective in enforcing a wide range of boundary conditions while preserving satisfactory convergence characteristics. The modular structure of the framework further enabled systematic comparisons among different kinematic models, ranging from the classical Sanders–Koiter theory to higher-order five-, six-, and seven-parameter formulations. In particular, the seven-parameter model incorporating the Enhanced Assumed Strain concept demonstrated an improved capability to mitigate thickness-related and Poisson locking effects, leading to more reliable predictions for moderately thick shells.

Numerical studies involving functionally graded materials and laminated orthotropic composites confirmed the versatility and robustness of the proposed framework. The computed natural frequencies and mode shapes exhibited an excellent agreement with three-dimensional finite element solutions. These results highlight the ability of the proposed approach to capture the main dynamic characteristics of complex shell structures while retaining computational efficiency, making it a suitable tool for advanced vibration analyses of shell components in engineering applications.

Although the present work is restricted to linear free vibration analysis, the proposed framework is well suited for extensions to geometrically and materially nonlinear shell problems, including nonlinear statics and dynamics. In this context, the Enhanced Assumed Strain approach is particularly attractive, as it improves the predictive performance of the formulation without increasing the number of degrees of freedom. By enriching the strain field rather than the displacement approximation, the method enhances accuracy while preserving a reduced system size, which is a key advantage in nonlinear analyses where the computational cost is strongly influenced by the number of degrees of freedom.

CRediT authorship contribution statement

F.A.X.C. Pinho: Writing – original draft, Validation, Supervision, Software, Methodology, Formal analysis, Conceptualization. **F.M.A. Silva:** Writing – review & editing, Conceptualization. **F.A.C. Monteiro:** Writing – review & editing. **M. Amabili:** Writing – review & editing. **C.G. Pitaluga:** Writing – review & editing, Validation.

Funding

This work was supported by the Foundation for Research Support of Goiás State (FAPEG), grant number 202510267000673 (Caleb Gomes Pitaluga); and the National Council for Scientific and Technological Development (CNPq), grant number 303646/2024-1 (Frederico Martins Alves da Silva).

Declaration of competing interest

The authors declare that they have no known competing financial interests or personal relationships that could have appeared to influence the work reported in this paper.

Appendix. Geometric properties of the shell

A.1. Mid-surface differential geometry

Let $\mathbf{R} = \mathbf{R}(\xi^1, \xi^2)$ denote the position vector of an arbitrary point on the mid-surface of the shell in the reference configuration, parametrized by the curvilinear coordinates ξ^1 and ξ^2.

The vectors

$$\mathbf{M}_1 = \frac{\partial \mathbf{R}}{\partial \xi^1} \qquad \mathbf{M}_2 = \frac{\partial \mathbf{R}}{\partial \xi^2} \qquad \mathbf{M}_3 = \frac{\mathbf{M}_1 \times \mathbf{M}_2}{|\mathbf{M}_1 \times \mathbf{M}_2|} \tag{A.1}$$

define the natural (covariant) basis of the mid-surface in the reference configuration. The first two vectors are tangent to the surface along the parametric directions, whereas $\mathbf{M}_3$ is the unit normal. The reciprocal (contravariant) basis $\mathbf{M}^1$, $\mathbf{M}^2$, and $\mathbf{M}^3$ satisfies

$$\mathbf{M}_i \cdot \mathbf{M}^j = \delta_i^j \tag{A.2}$$

These bases are used to express all geometric quantities of the shell in the reference configuration.

The metric tensor, expressed in covariant, contravariant, and mixed forms, characterizes the local inner products of the basis vectors:

$$G_{ij} = \mathbf{M}_i \cdot \mathbf{M}_j \qquad G^{ij} = \mathbf{M}^i \cdot \mathbf{M}^j \qquad G^i_j = \mathbf{M}^i \cdot \mathbf{M}_j = \delta^i_j \tag{A.3}$$

The curvature tensor

$$\begin{aligned} K_{\alpha\beta} &= \mathbf{M}_\alpha \cdot \frac{\partial \mathbf{M}_3}{\partial \xi^\beta} = -\mathbf{M}_3 \cdot \frac{\partial \mathbf{M}_\alpha}{\partial \xi^\beta} = -\mathbf{M}_3 \cdot \frac{\partial \mathbf{M}_\beta}{\partial \xi^\alpha} \\ K^\alpha_{\cdot\beta} &= \mathbf{M}^\alpha \cdot \frac{\partial \mathbf{M}^3}{\partial \xi^\beta} = -\mathbf{M}^3 \cdot \frac{\partial \mathbf{M}^\alpha}{\partial \xi^\beta} \end{aligned} \tag{A.4}$$

captures the variation of the surface normal along the parametric directions. The Christoffel symbols

$$\Gamma^\gamma_{\alpha\beta} = \mathbf{M}^\gamma \cdot \frac{\partial \mathbf{M}_\alpha}{\partial \xi^\beta} \qquad \Gamma^\alpha_{\gamma\beta} = -\mathbf{M}_\gamma \cdot \frac{\partial \mathbf{M}^\alpha}{\partial \xi^\beta} \tag{A.5}$$

encode the connection on the surface and appear naturally in expressions for covariant derivatives.

Using the curvature tensor together with the Christoffel symbols, the Gauss and Weingarten relations

$$\begin{aligned} \frac{\partial \mathbf{M}_3}{\partial \xi^\beta} &= K^\alpha_{\cdot\beta}\mathbf{M}_\alpha \qquad & \frac{\partial \mathbf{M}_\alpha}{\partial \xi^\beta} &= \Gamma^\gamma_{\alpha\beta}\mathbf{M}_\gamma - K_{\alpha\beta}\mathbf{M}_3 \\ \frac{\partial \mathbf{M}^3}{\partial \xi^\beta} &= K_{\alpha\beta}\mathbf{M}^\alpha \qquad & \frac{\partial \mathbf{M}^\alpha}{\partial \xi^\beta} &= -\Gamma^\alpha_{\gamma\beta}\mathbf{M}^\gamma - K^\alpha_{\cdot\beta}\mathbf{M}_3 \end{aligned} \tag{A.6}$$

fully describe the differential geometry of the mid-surface in the reference configuration.

A.2. Tensorial description of the shell geometry

The position vector of an arbitrary point within the shell is given in terms of the mid-surface and the normal direction, as in (1). Partial derivatives of the shell position vector with respect to the curvilinear coordinates

$$\frac{\partial \mathbf{X}}{\partial \xi^\alpha} = \mathbf{M}_\alpha + \xi^3 \frac{\partial \mathbf{M}_3}{\partial \xi^\alpha} \qquad \frac{\partial \mathbf{X}}{\partial \xi^3} = \mathbf{M}_3 \tag{A.7}$$

yield the covariant base vectors of the shell, which incorporate the mid-surface curvature via the curvature tensor $K_{\alpha\beta}$. Equivalently, this can be expressed as

$$\frac{\partial \mathbf{X}}{\partial \xi^i} = \bar{\mathbf{M}}_i \tag{A.8}$$

where

$$\bar{\mathbf{M}}_\alpha = \mathbf{X}_{,\alpha} = \left(\delta^\beta_\alpha + \xi^3 K^\beta_{\cdot\alpha}\right)\mathbf{M}_\beta \qquad \bar{\mathbf{M}}_3 = \mathbf{X}_{,3} = \mathbf{M}_3 \tag{A.9}$$

Consider the shift tensor

$$\boldsymbol{\Upsilon} = \Upsilon^\beta_{\cdot\alpha}\mathbf{M}_\beta \otimes \mathbf{M}^\alpha \qquad \Upsilon^\beta_{\cdot\alpha} = \delta^\beta_\alpha + \xi^3 K^\beta_{\cdot\alpha} \tag{A.10}$$

to describe the geometry of a shell at a distance ξ^3 from the mid-surface. This tensor defines a linear mapping from the natural covariant basis of the mid-surface $\mathbf{M}_\alpha$ to the covariant basis of the shell

$$\bar{\mathbf{M}}_\alpha = \boldsymbol{\Upsilon} \cdot \mathbf{M}_\alpha \tag{A.11}$$

whose components are $\Upsilon^{\beta}_{\cdot\alpha} = \delta^\beta_\alpha + \xi^3 K^{\beta}_{\cdot\alpha}$, then $\bar{\mathbf{M}}_\alpha = \Upsilon^{\beta}_{\cdot\alpha}\mathbf{M}_\beta$. Physically, the tensor $\boldsymbol{\Upsilon}$ encodes how the covariant basis vectors stretch and rotate as one moves along the thickness direction ξ^3 due to the curvature of the mid-surface. Its components reduce to the identity at the mid-surface, and they vary linearly with ξ^3 following the curvature tensor $K^{\beta}_{\cdot\alpha}$. This simple linear relation allows us to proper map geometric quantities from the mid-surface to any point within the shell. Similarly, the reciprocal (contravariant) basis of the shell $\bar{\mathbf{M}}^\alpha = \boldsymbol{\Lambda} \cdot \mathbf{M}^\alpha$ can be related to the mid-surface contravariant basis $\mathbf{M}^\alpha$ through the tensor $\boldsymbol{\Lambda} = \Lambda^{\cdot\alpha}_{\beta}\mathbf{M}^\beta \otimes \mathbf{M}_\alpha$, so that $\bar{\mathbf{M}}^\alpha = \Lambda^{\cdot\alpha}_{\beta}\mathbf{M}^\beta$.

The components $\Lambda^{\cdot\alpha}_{\beta}$ are defined as follows. First, the tensor $\boldsymbol{\Lambda}$ is set as the transpose inverse of $\boldsymbol{\Upsilon}$, i.e. $[\Lambda]^T = [\Upsilon]^{-1}$, ensuring that the contravariant and covariant bases remain mutually orthogonal throughout the shell. This inverse relationship is crucial for defining the metric tensor and all derived geometric quantities consistently across the thickness of the shell. Second, the inverse of the shift tensor

$$\boldsymbol{\Upsilon}^{-1} = (\mathbf{G} + \xi^3\mathbf{K})^{-1} = \sum_{n=0}^{\infty}(-1)^n(\xi^3\mathbf{K})^n = \boldsymbol{\Lambda}^T \tag{A.12}$$

is set as a power-series around $\xi^3 = 0$, according to the Neumann series. Then,

$$\Lambda^{\cdot\alpha}_{\beta} = \delta^\alpha_\beta - \xi^3\, K^{\alpha}_{\cdot\beta} + (\xi^3)^2\, K^{\alpha}_{\cdot\gamma}K^{\gamma}_{\cdot\beta} - (\xi^3)^3\, K^{\alpha}_{\cdot\gamma}K^{\gamma}_{\cdot\delta}K^{\delta}_{\cdot\beta} + \cdots \tag{A.13}$$

The Gauss–Weingarten relations, which describe the variation of the basis vectors along the surface,

$$\begin{aligned}
\frac{\partial\bar{\mathbf{M}}_3}{\partial\xi^\beta} &= \bar{K}^{\alpha}_{\cdot\beta}\bar{\mathbf{M}}_\alpha &\qquad \frac{\partial\bar{\mathbf{M}}_\alpha}{\partial\xi^\beta} &= \bar{\Gamma}^{\gamma}_{\alpha\beta}\bar{\mathbf{M}}_\gamma - \bar{K}_{\alpha\beta}\bar{\mathbf{M}}_3\\
\frac{\partial\bar{\mathbf{M}}^3}{\partial\xi^\beta} &= \bar{K}_{\alpha\beta}\bar{\mathbf{M}}^\alpha &\qquad \frac{\partial\bar{\mathbf{M}}^\alpha}{\partial\xi^\beta} &= -\bar{\Gamma}^{\alpha}_{\gamma\beta}\bar{\mathbf{M}}^\gamma - \bar{K}^{\alpha}_{\cdot\beta}\bar{\mathbf{M}}_3
\end{aligned} \tag{A.14}$$

can also be extended from the mid-surface to the shell. Importantly, while the mid-surface bases $\mathbf{M}_i$ and $\mathbf{M}^i$ are independent of ξ^3, the shell bases $\bar{\mathbf{M}}_i$ and $\bar{\mathbf{M}}^i$ explicitly depend on the thickness coordinate. This dependence is governed by the curvature of the mid-surface through the relations

$$\frac{\partial\bar{\mathbf{M}}_\alpha}{\partial\xi^3} = \bar{K}^{\beta}_{\cdot\alpha}\bar{\mathbf{M}}_\beta \qquad \frac{\partial\bar{\mathbf{M}}^\alpha}{\partial\xi^3} = -\bar{K}^{\alpha}_{\cdot\beta}\bar{\mathbf{M}}^\beta. \tag{A.15}$$

These expressions show that the change of the basis vectors along the thickness direction is directly linked to the curvature of the mid-surface. They allow for a natural extension of the differential geometry from the mid-surface to the full shell, which is essential for formulating the kinematics and strains in shell theory.

Finally, the metric tensors

$$\bar{G}_{\alpha\beta} = \Upsilon^{\theta}_{\cdot\alpha}\Upsilon^{\lambda}_{\cdot\beta}G_{\theta\lambda} \qquad \bar{G}^{\alpha\beta} = \Lambda^{\cdot\alpha}_{\theta}\Lambda^{\cdot\beta}_{\lambda}G^{\theta\lambda} \qquad \bar{G}^{\alpha}_{\beta} = \Lambda^{\cdot\alpha}_{\theta}\Upsilon^{\lambda}_{\cdot\beta}G^{\theta}_{\lambda} \tag{A.16}$$

the Christoffel symbols

$$\bar{\Gamma}^{\gamma}_{\beta\alpha} = \Lambda^{\cdot\gamma}_{\sigma}\Upsilon^{\nu}_{\cdot\beta}\Gamma^{\sigma}_{\nu\alpha} + \Lambda^{\cdot\gamma}_{\nu}\Upsilon^{\nu}_{\cdot\beta,\alpha} \tag{A.17}$$

and the curvature tensor

$$\bar{K}_{\beta\alpha} = \Upsilon^{\theta}_{\cdot\beta}K_{\theta\alpha} \qquad \bar{K}^{\beta}_{\cdot\alpha} = \Lambda^{\cdot\beta}_{\theta}K^{\theta}_{\cdot\alpha} \tag{A.18}$$

are expressed in terms of the mid-surface tensors and the shift tensors $\boldsymbol{\Upsilon}$ and $\boldsymbol{\Lambda}$. In this way, the full geometry of the shell is completely described in terms of the mid-surface geometry and the curvature mapping, providing a consistent framework for strain and stress analysis across the shell thickness.

A.3. Covariant derivatives of the displacement vector

Let the displacement vector

$$\mathbf{U} = \mathbf{U}(\xi^1, \xi^2, \xi^3) \tag{A.19}$$

parametrized by the curvilinear coordinates ξ^1, ξ^2, ξ^3. It can be decomposed in different bases as

$$\mathbf{U} = \bar{U}_i\bar{\mathbf{M}}^i = \bar{U}^i\bar{\mathbf{M}}_i = U_i\mathbf{M}^i = U^i\mathbf{M}_i. \tag{A.20}$$

It follows that $U_3 = U^3 = \bar{U}_3 = \bar{U}^3$.

The covariant derivatives of $\mathbf{U}$

$$\frac{\partial\mathbf{U}}{\partial\xi^i} = \bar{U}_{j\|i}\bar{\mathbf{M}}^j = \bar{U}^j\,\|_i\,\bar{\mathbf{M}}_j = U_{j|i}\mathbf{M}^j = U^j|_i\mathbf{M}_j \tag{A.21}$$

can be expressed in terms of the respective bases, where the double bar $\|$ denotes covariant differentiation with respect to the shell basis $\bar{\mathbf{M}}_i$, and the single bar $|$ denotes covariant differentiation with respect to the mid-surface basis $\mathbf{M}_i$.

A.3.1. Covariant derivatives along the mid-surface

In the mid-surface basis, the covariant derivatives

$$U_{\sigma|\alpha} = U_{\sigma,\alpha} - \Gamma^{\tau}_{\sigma\alpha}U_\tau + K_{\alpha\sigma}U_3 \qquad U_{3|\alpha} = U_{3,\alpha} - K^{\tau}_{\cdot\alpha}U_\tau \tag{A.22}$$

account for the surface curvature and connection coefficients. The derivatives

$$U_{\alpha|3} = U_{\alpha,3} \qquad U_{3|3} = U_{3,3} \tag{A.23}$$

along the thickness direction can be simplified because the mid-surface basis vectors are independent of ξ^3. For the contravariant components in the mid-surface basis, the corresponding covariant derivatives are

$$\begin{aligned}
U^\sigma|_\alpha &= U^\sigma_{,\alpha} - \Gamma^{\sigma}_{\alpha\tau}U^\tau + K^{\sigma}_{\cdot\alpha}U_3\\
U^3|_\alpha &= U^3_{,\alpha} - K_{\tau\alpha}U^\tau\\
U^\alpha|_3 &= U^\alpha_{,3}\\
U^3|_3 &= U^3_{,3}
\end{aligned} \tag{A.24}$$

A.3.2. Covariant derivatives in the shell basis

In the shell basis, the derivatives along the mid-surface directions are

$$\bar{U}_{\sigma\|\alpha} = \bar{U}_{\sigma,\alpha} - \bar{\Gamma}^{\tau}_{\sigma\alpha}\bar{U}_\tau + \bar{K}_{\alpha\sigma}\bar{U}_3 \qquad \bar{U}_{3\|\alpha} = \bar{U}_{3,\alpha} - \bar{K}^{\tau}_{\cdot\alpha}\bar{U}_\tau \tag{A.25}$$

Covariant derivatives along the thickness direction

$$\frac{\partial\mathbf{U}}{\partial\xi^3} = \frac{\partial}{\partial\xi^3}\left(\bar{U}_\alpha\bar{\mathbf{M}}^\alpha + \bar{U}_3\bar{\mathbf{M}}^3\right) = \bar{U}_{\alpha,3}\bar{\mathbf{M}}^\alpha - \bar{U}_\theta\bar{K}^{\theta}_{\cdot\alpha}\bar{\mathbf{M}}^\alpha + \bar{U}_{3,3}\bar{\mathbf{M}}^3 \tag{A.26}$$

must account for the dependence of $\bar{\mathbf{M}}^\alpha$ on ξ^3, so that

$$\bar{U}_{\alpha\|3} = \bar{U}_{\alpha,3} - \bar{K}^{\theta}_{\cdot\alpha}\bar{U}_\theta \qquad \bar{U}_{3\|3} = \bar{U}_{3,3} \tag{A.27}$$

A.3.3. Relations between shell and mid-surface covariant derivatives

Finally, the shift tensors $\boldsymbol{\Upsilon}$ and $\boldsymbol{\Lambda}$ allow expressing shell derivatives in terms of mid-surface derivatives:

$$\begin{aligned}
&\bar{U}_{\alpha\|\beta} = \Upsilon^{\theta}_{\cdot\alpha}U_{\theta|\beta} &\quad &\bar{U}_{\alpha\|3} = \Upsilon^{\theta}_{\cdot\alpha}U_{\theta|3} &\quad &\bar{U}_{3\|\alpha} = U_{3|\alpha} &\quad &\bar{U}_{3\|3} = U_{3,3}\\
&\bar{U}^\alpha\,\|_\beta = \Lambda^{\cdot\alpha}_{\theta}U^\theta|_\beta &\quad &\bar{U}^\alpha\,\|_3 = \Lambda^{\cdot\alpha}_{\theta}U^\theta|_3 &\quad &\bar{U}^3\,\|_\alpha = U^3|_\alpha &\quad &\bar{U}^3\,\|_3 = U^3|_3
\end{aligned} \tag{A.28}$$

This formulation provides a consistent framework to compute covariant derivatives of the displacement vector in any shell-related basis, while naturally accounting for the geometry of the mid-surface.

Data availability

Research Link Provided

ShellPy: A Python framework for general shell analysis (Original data) (GitHub)

References

[1] Naghdi PM. The theory of shells and plates. In: Linear theories of elasticity and thermoelasticity: linear and nonlinear theories of rods, plates, and shells. Berlin, Heidelberg: Springer Berlin Heidelberg; 1973, p. 425–640. http://dx.doi.org/10.1007/978-3-662-39776-3_5.

[2] Qatu MS. Vibration of Laminated Shells and Plates. Oxford: Academic Press; 2004.

[3] Punera D, Kant T. A critical review of the existing literature on the topic of fg shells. Compos Struct 2019;210:787–809. http://dx.doi.org/10.1016/j.compstruct.2018.11.084.

[4] Viola E, Tornabene F, Fantuzzi N. General higher-order shear deformation theories for the free vibration analysis of completely doubly-curved laminated shells and panels. Compos Struct 2013;95:639–66. http://dx.doi.org/10.1016/j.compstruct.2012.08.005.

[5] Kreja I, Schmidt R. Large rotations in first-order shear deformation FE analysis of laminated shells. Int J Non-Linear Mech 2006;41(1):101–23. http://dx.doi.org/10.1016/j.ijnonlinmec.2005.06.009.

[6] Nguyen T-K, Sab K, Bonnet G. Shear correction factors for functionally graded plates. Mech Adv Mater Struct 2007;14(8):567–75. http://dx.doi.org/10.1080/15376490701672575.

[7] Amabili M. Nonlinear vibrations and stability of shells and plates. Cambridge: Cambridge University Press; 2008.

[8] Amabili M. Nonlinear Mechanics of Shells and Plates in Composite, Soft and Biological Materials. Cambridge: Cambridge University Press; 2018.

[9] Reinoso J, Blázquez A. Application and finite element implementation of 7-parameter shell element for geometrically nonlinear analysis of layered CFRP composites. Compos Struct 2016;139:263–76. http://dx.doi.org/10.1016/j.compstruct.2015.12.009.

[10] Carrera E, Brischetto S. Analysis of thickness locking in classical, refined and mixed multilayered plate theories. Compos Struct 2008;82(4):549–62. http://dx.doi.org/10.1016/j.compstruct.2007.02.002.

[11] Braun M, Bischoff M, Ramm E. Nonlinear shell formulations for complete three-dimensional constitutive laws including composites and laminates. Comput Mech 1994;15:1–18. http://dx.doi.org/10.1007/BF00350285.

[12] Carrera E. Theories and finite elements for multilayered plates and shells: a unified compact formulation with numerical assessment and benchmarking. Arch Comput Methods Eng 2003;10(3):215–96.

[13] Carrera E, Cinefra M, Petrolo M, Zappino E. Finite Element Analysis of Structures Through Unified Formulation. John Wiley & Sons; 2014.

[14] Qatu MS, Leissa AW. Natural frequencies for cantilevered doubly-curved laminated composite shallow shells. Compos Struct 1991;17(3):227–55. http://dx.doi.org/10.1016/0263-8223(91)90053-2.

[15] Thang PT, Kim C, Jang H, Kim T, Kim J. Free vibration characteristics of honeycomb sandwich cylindrical shells reinforced with graphene nanoplatelets/polymer coatings. Aerosp Sci Technol 2025;156:109744. http://dx.doi.org/10.1016/j.ast.2024.109744.

[16] Liu J, Ji C, Ye W, Gan L, Qin L, Zang Q, Wang H. Static and vibration analyses of laminated conical shells under various boundary conditions using a modified scaled boundary finite element method. Comput Math Appl 2025;177:147–66. http://dx.doi.org/10.1016/j.camwa.2024.11.024.

[17] Ismail MS, Mahmud J, Ifayefunmi O, Purbolaksono J. Buckling failures in curved shell structures: a comprehensive review of theory, design, and applications. J Braz Soc Mech Sci Eng 2026;48(2):83.

[18] Rafiefar M, Moeenfard H. Analytical modeling of variable thickness cylindrical shallow shells using extended kantorovich method. Eur J Mech A Solids 2022;96:104727. http://dx.doi.org/10.1016/j.euromechsol.2022.104727.

[19] Rafiefar M, Moeenfard H. Vibration modeling of variable thickness cylindrical shallow shells using extended kantorovich method. Structures 2024;70:107554. http://dx.doi.org/10.1016/j.istruc.2024.107554.

[20] Hadrich A, Zghal S, Koubaa S, Bouaziz Z. Free vibration of functionally graded porous perforated solid structures with complex shaped holes. Int J Solids Struct 2025;319:113449. http://dx.doi.org/10.1016/j.ijsolstr.2025.113449.

[21] Gao D, Zhao B. Analytical solution for laminated axisymmetric spherical shell based on state space approach and Legendre polynomials. Thin-Walled Struct 2026;220:114350. http://dx.doi.org/10.1016/j.tws.2025.114350.

[22] Hong C-C. Advanced dynamic responses of thick FGM spherical shells analyzed using TSDT under thermal vibration. Computation 2025;13(10). http://dx.doi.org/10.3390/computation13100245.

[23] Tamnar RB, Sayyad AS. A refined shell theory considering the effects of transverse normal strain for the analysis of functionally graded porous shallow shells with double curvature. Mech Adv Mater Struct 2025;32(6):1258–74. http://dx.doi.org/10.1080/15376494.2024.2361462.

[24] Sun Y, Zhou Z, Lai P, et al. Isogeometric analysis-based buckling optimization framework for grid-stiffened shells using asymptotic homogenization method and Rayleigh–ritz method. Struct Multidiscip Optim 2022;65:330. http://dx.doi.org/10.1007/s00158-022-03441-4.

[25] Leonetti L, Magisano D, Garcea G. Large rotation isogeometric shell model for alternating stiff/soft curved laminates including warping and interlayer thickness change. Comput Methods Appl Mech Engrg 2024;424:116908. http://dx.doi.org/10.1016/j.cma.2024.116908.

[26] Zhou Z, Sun Y, Li X, Zhou Y, Tian K, Hao P, Wang B. Shape and size optimization framework of stiffened shell using isogeometric analysis. Thin-Walled Struct 2024;204:112311. http://dx.doi.org/10.1016/j.tws.2024.112311.

[27] Yan K, Wu Y, Zhu Q, Khoo BC. A coupled immersed boundary method and isogeometric shell analysis for fluid–structure interaction of flexible and lightweight shells in high-Reynolds number flows. Comput Methods Appl Mech Engrg 2025;439:117898. http://dx.doi.org/10.1016/j.cma.2025.117898.

[28] Liu T, Xu W, Wang Y, Cai S, Hu X, Gu J. Isogeometric Reissner–mindlin shell analysis for post-buckling of piezoelectric laminated shell panels. Eng Anal Bound Elem 2025;172:106114. http://dx.doi.org/10.1016/j.enganabound.2025.106114.

[29] Provatidis CG, Sevilla R, Schillinger D, et al. Revisiting transfinite elements: Unifying element formulations for IGA, SEM, NEFEM, p-FEM and h-FEM. Arch Comput Methods Eng 2026;33:1795–840. http://dx.doi.org/10.1007/s11831-025-10351-3.

[30] Hachemi M, Guenanou A, Touahra F, et al. A layer-wise p-FEM for buckling and free vibration analysis of laminated FG-CNTRC sandwich plates. J Vib Eng Technol 2026;14:194. http://dx.doi.org/10.1007/s42417-026-02404-z.

[31] Azizi N, Dornisch W. A spectral finite element Reissner–mindlin shell formulation with NURBS-based geometry definition. Comput Mech 2024;74:537–59. http://dx.doi.org/10.1007/s00466-024-02444-w.

[32] Lotfan S, Cigeroglu E. Reduced-order spectral Chebyshev models for geometrically nonlinear vibrations of thin-walled structures. Nonlinear Dynam 2025;113:25753–85. http://dx.doi.org/10.1007/s11071-025-11434-3.

[33] Guarino G, Milazzo A. A discontinuous Galerkin formulation for nonlinear analysis of multilayered shells refined theories. Int J Mech Sci 2023;255:108426. http://dx.doi.org/10.1016/j.ijmecsci.2023.108426.

[34] Gulizzi V, Benedetti I, Milazzo A. High-order accurate transient and free-vibration analysis of plates and shells. J Sound Vib 2024;587:118479. http://dx.doi.org/10.1016/j.jsv.2024.118479.

[35] Xu H, Wang Y, Xu Z, Yu X. Gegenbauer-ritz method for free vibration analysis of rotating functionally graded graphene reinforced porous composite stepped cylindrical shells with arbitrary boundary conditions. Eng Struct 2024;303:117555. http://dx.doi.org/10.1016/j.engstruct.2024.117555.

[36] Büchter N, Ramm E, Roehl D. Three-dimensional extension of non-linear shell formulation based on the enhanced assumed strain concept. Internat J Numer Methods Engrg 1994;37(15):2551–68. http://dx.doi.org/10.1002/nme.1620371504.

[37] Xia ZX, Touzé C, Cong Y, Gu S, Feng Z-Q. Reduced order modelling for shell finite element structures using the direct parametrisation of invariant manifolds. Thin-Walled Struct 2026;220:114329. http://dx.doi.org/10.1016/j.tws.2025.114329.

[38] Pinho F. Shellpy: A python library for shell analysis. 2025, URL https://github.com/flaviopinho/shellpy.

[39] Pinho FAXC, Del Prado ZJGN, Silva FMA. On the free vibration problem of thin shallow and non-shallow shells using tensor formulation. Eng Struct 2021;244:112807. http://dx.doi.org/10.1016/j.engstruct.2021.112807.

[40] Pinho FAXC, Del Prado ZJGN, Silva FMA. Nonlinear static analysis of thin shallow and non-shallow shells using tensor formulation. Eng Struct 2022;253:113674. http://dx.doi.org/10.1016/j.engstruct.2021.113674.

[41] Pinho FAXC, Amabili M, Del Prado ZJGN, Silva FMA. Nonlinear free vibration analysis of doubly curved shells. Nonlinear Dynam 2023;111:21535–55. http://dx.doi.org/10.1007/s11071-023-08963-0.

[42] Pinho FAXC, Amabili M, Del Prado ZJGN, da Silva FMA. Nonlinear forced vibration analysis of doubly curved shells via the parameterization method for invariant manifold. Nonlinear Dynam 2024;112:20677–701. http://dx.doi.org/10.1007/s11071-024-10135-7.

[43] Monteiro FAC, Lucena Neto E. Hierarchic sets of shape functions constructed from enriched Fourier series. Acta Mech 2024;235:671–90. http://dx.doi.org/10.1007/s00707-023-03767-0.

[44] Amabili M. Non-linearities in rotation and thickness deformation in a new third-order thickness deformation theory for static and dynamic analysis of isotropic and laminated doubly curved shells. Int J Non-Linear Mech 2015;69:109–28. http://dx.doi.org/10.1016/j.ijnonlinmec.2014.11.026.

[45] Amabili M, Reddy J. The nonlinear, third-order thickness and shear deformation theory for statics and dynamics of laminated composite shells. Compos Struct 2020;244:112265. http://dx.doi.org/10.1016/j.compstruct.2020.112265.

[46] Lee HG, Choi D-K, Kwon D, Park S. Refined shear correction factors for composite-layered FE shell elements to enhance the accuracy of their modal analysis results. Compos Struct 2026;377:119851. http://dx.doi.org/10.1016/j.compstruct.2025.119851.

[47] Matsunaga H. Free vibration and stability of functionally graded shallow shells according to a 2D higher-order deformation theory. Compos Struct 2008;84(2):132–46. http://dx.doi.org/10.1016/j.compstruct.2007.07.006.

[48] Das HS, Chakravorty D. Natural frequencies and mode shapes of composite conoids with complicated boundary conditions. J Reinf Plast Compos 2008;27(13):1397–419. http://dx.doi.org/10.1177/0731684407086508.